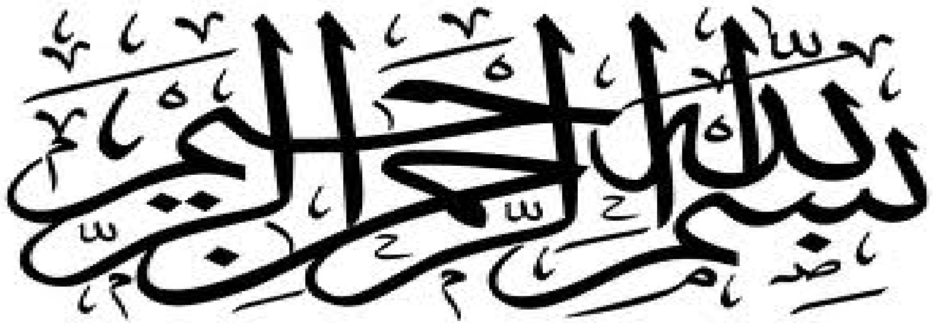

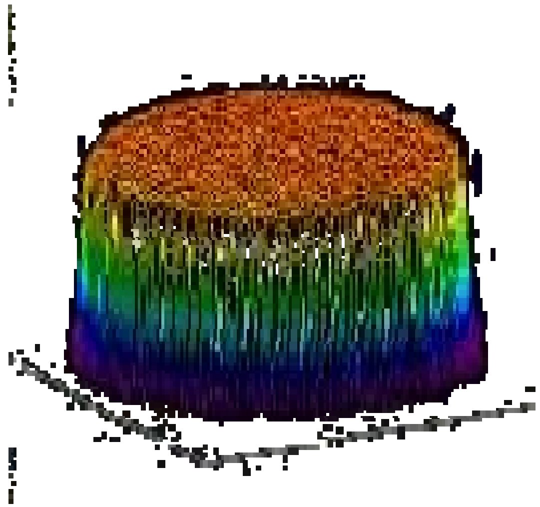

”The laser, a solution without a problem”

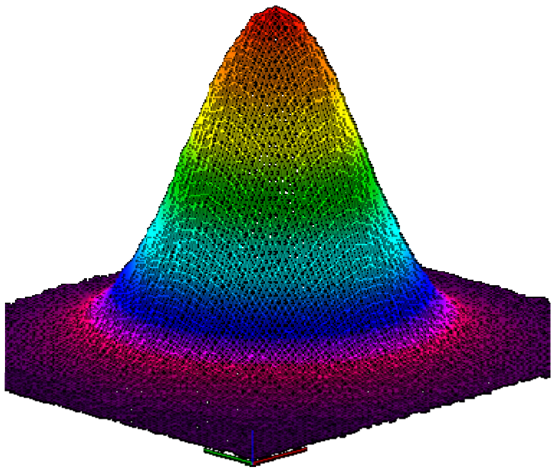

Anne Thorne, 1960

Summary of group activities

Laser Technology, Laser-matter Interaction and its Applications

Dr. Khaled Abdelsabour Elsayed
Physics Department
Faculty of Science
Cairo University

Outline

- ***What is Laser Induced Breakdown Spectroscopy (LIBS)?***

- **Basics of Laser Induced Breakdown Spectroscopy (LIBS)**

- **Design and construction of Q-Switched Nd: YAG Laser System for LIBS Measurements**

- **LIBS applications in Combustions, Archaeology,** ***biology, ..***

- ***Lidar systems:*** **Elastic Backscatter Lidar Signal to Noise Ratio Improvement for Daylight Operations**

- **Fabrication and size control of metal nanoparticles.**

What is LIBS?

LIBS is a physical technique applied to a typical problem of analytical chemistry, i.e. the determination of the elemental compositions of materials

Basics of Laser-Induced Breakdown Spectrometry (LIBS)

Elements of LIBS

1. Laser-sample interaction
2. Separation of material ⇒ Ablation
3. Plasma formation ⇒ Vapor ionization (breakdown)
4. Plasma spectral analysis ⇒ Emission spectrometry

1. Laser-sample interaction

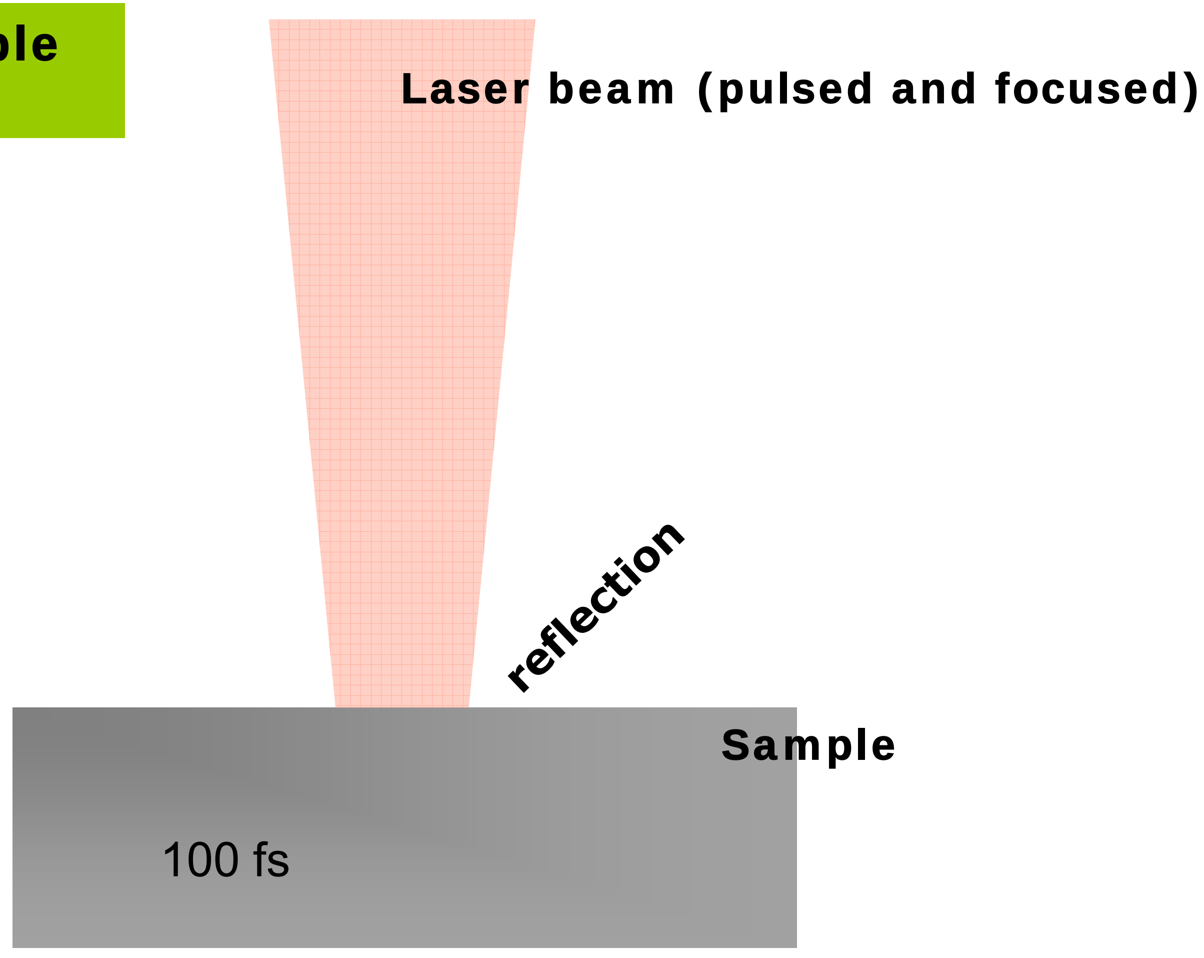

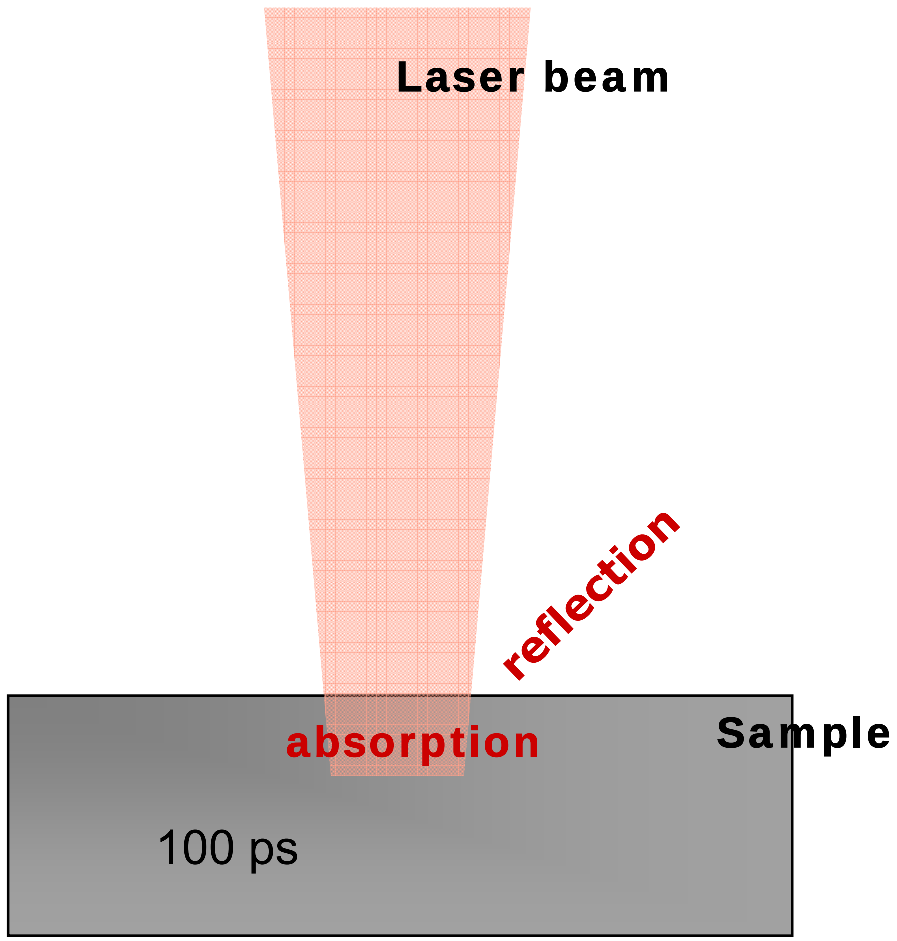
Laser beam
reflection
absorption
Sample
100 ps

2. Ablation

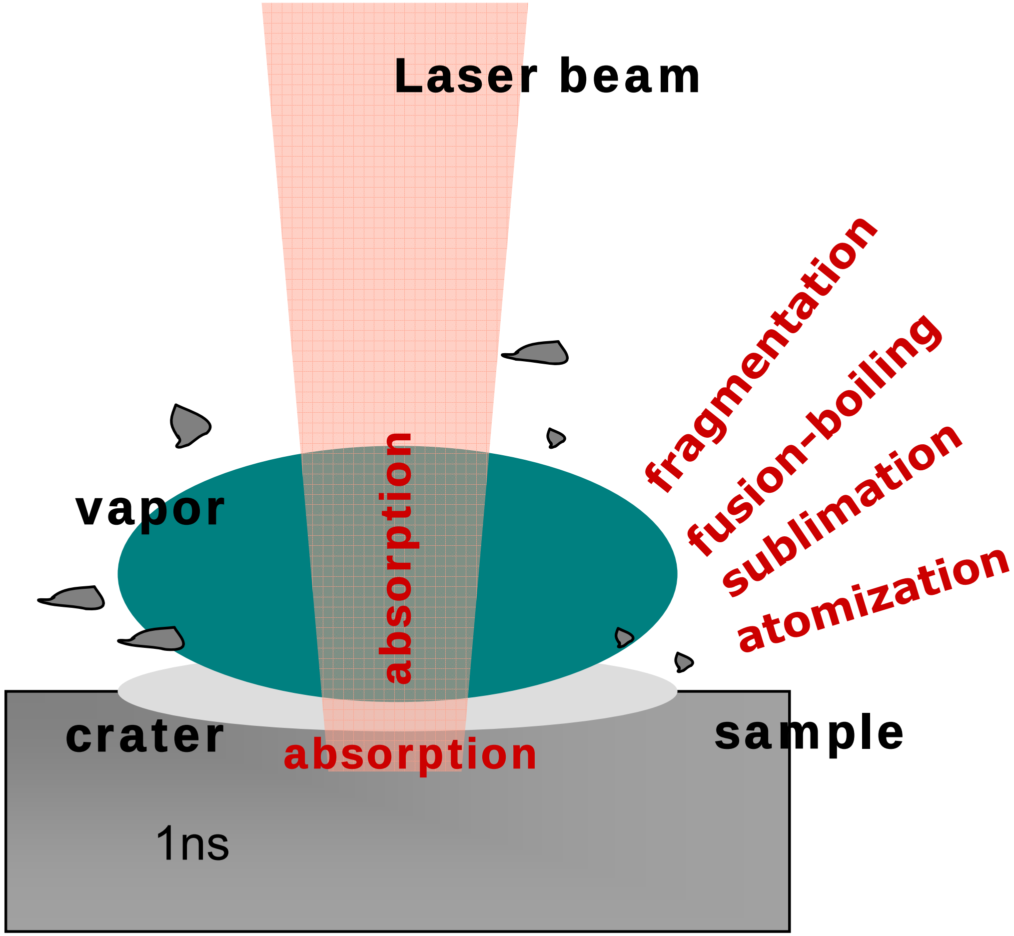

Laser beam
fragmentation
fusion-boiling
sublimation
atomization
vapor
absorption
crater
absorption
sample
1ns

3. Breakdown

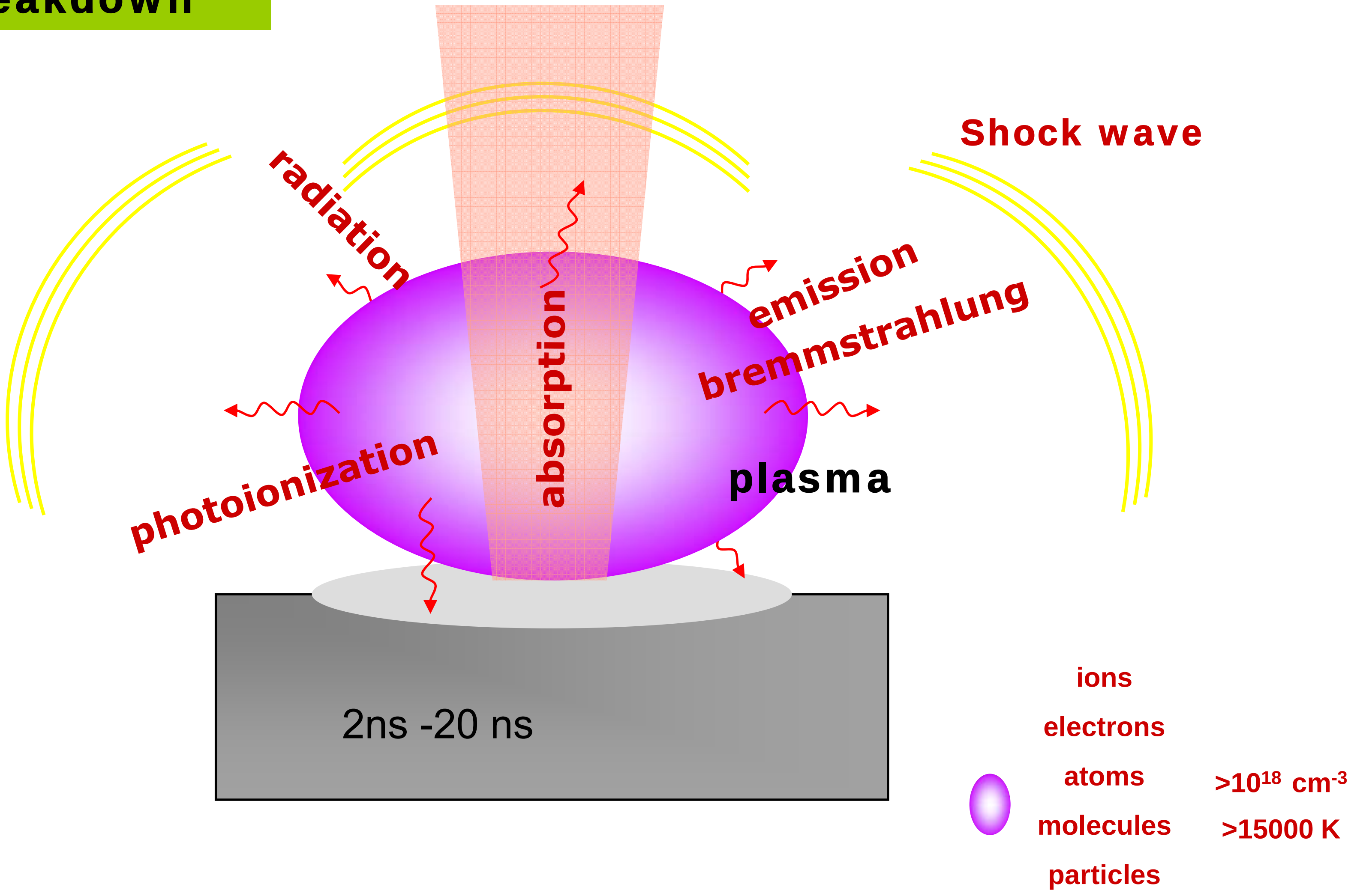
Shock wave
radiation
absorption
emission
bremmstrahlung
photoionization
plasma
2ns -20 ns
ions
electrons
atoms
molecules
particles
>10^18 cm^-3
>15000 K

Laser pulse ends

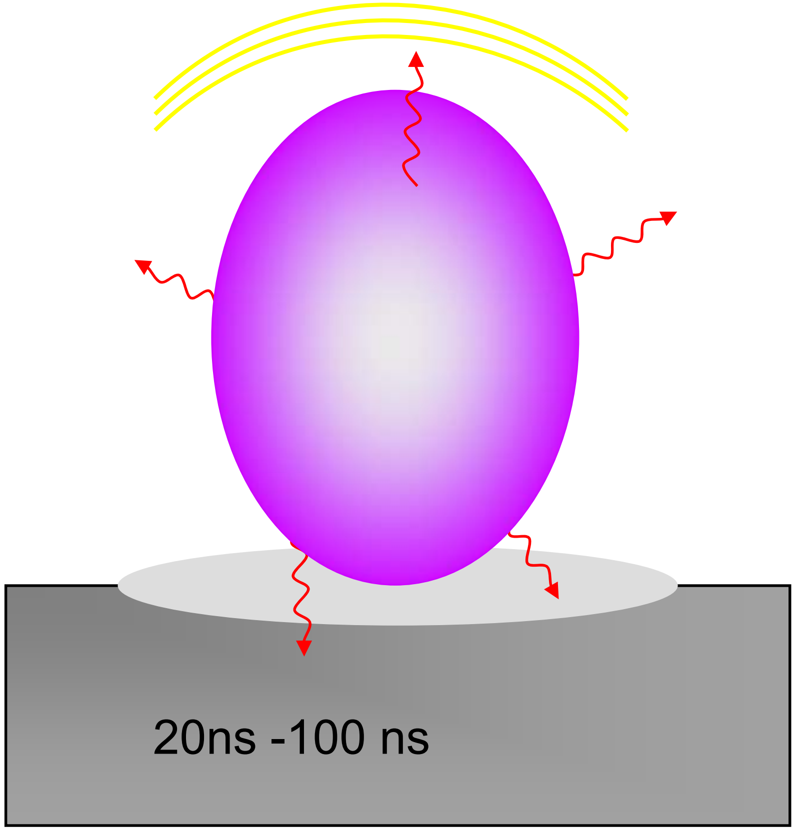

Plasma Cooling

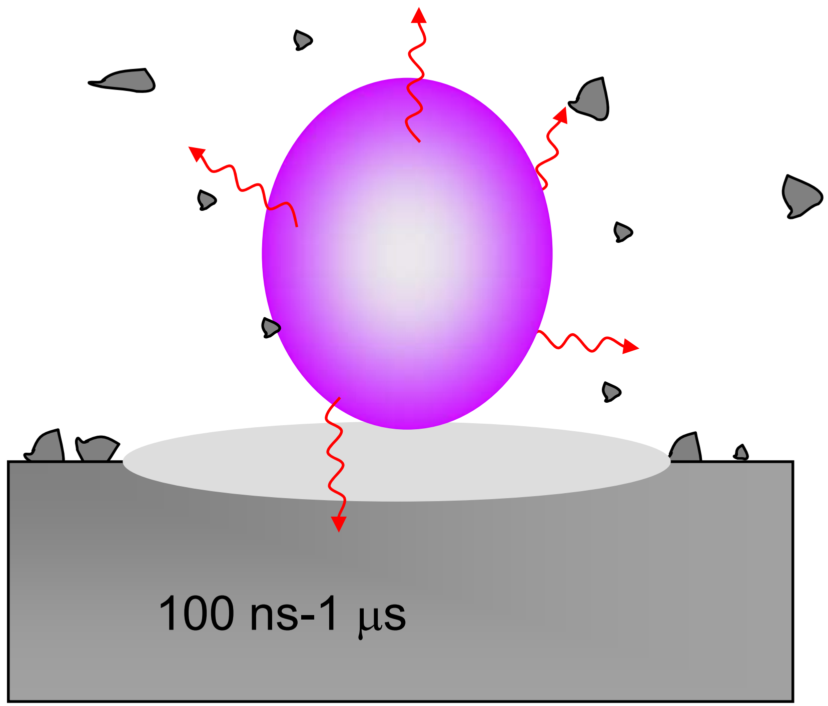

Plasma Cooling

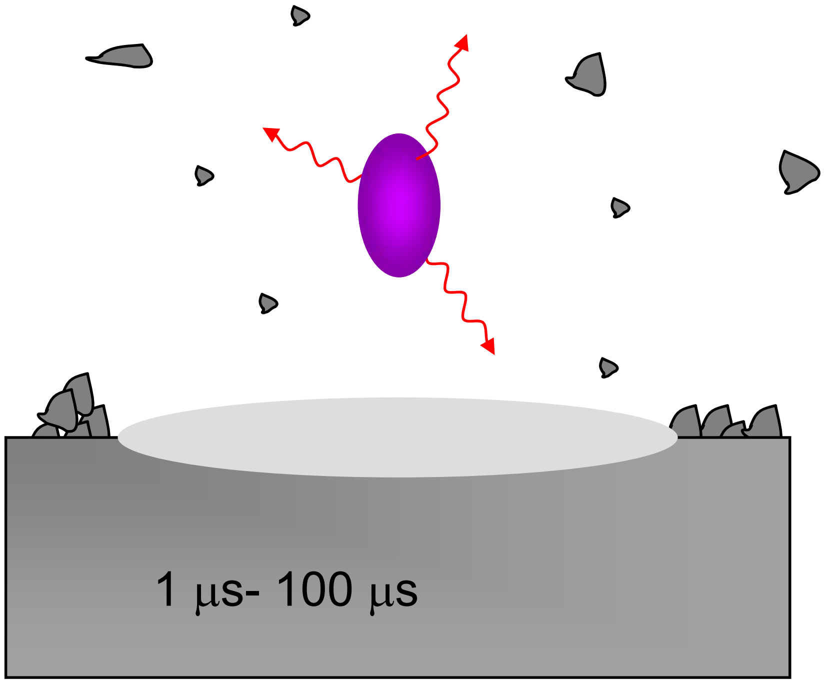

Plasma ends

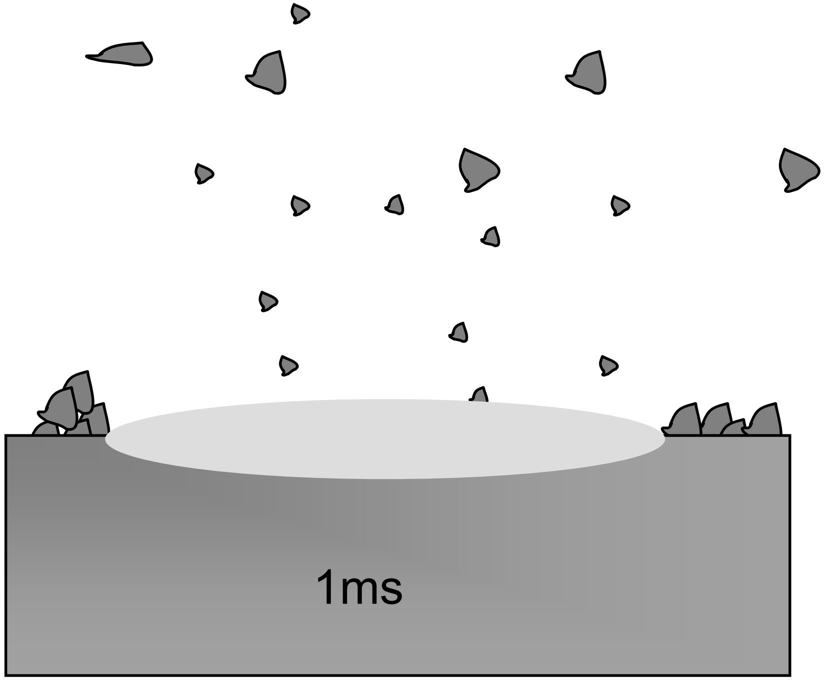

The evolution of the intensity emission from a laser induced plasma

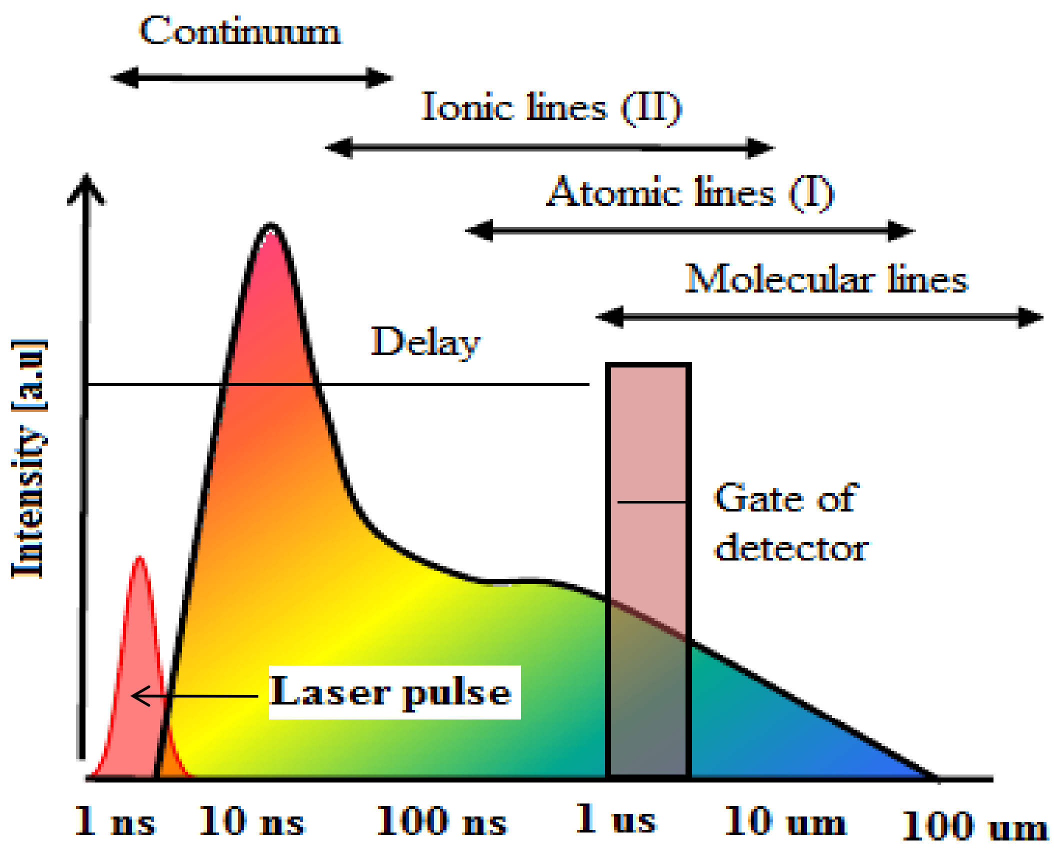

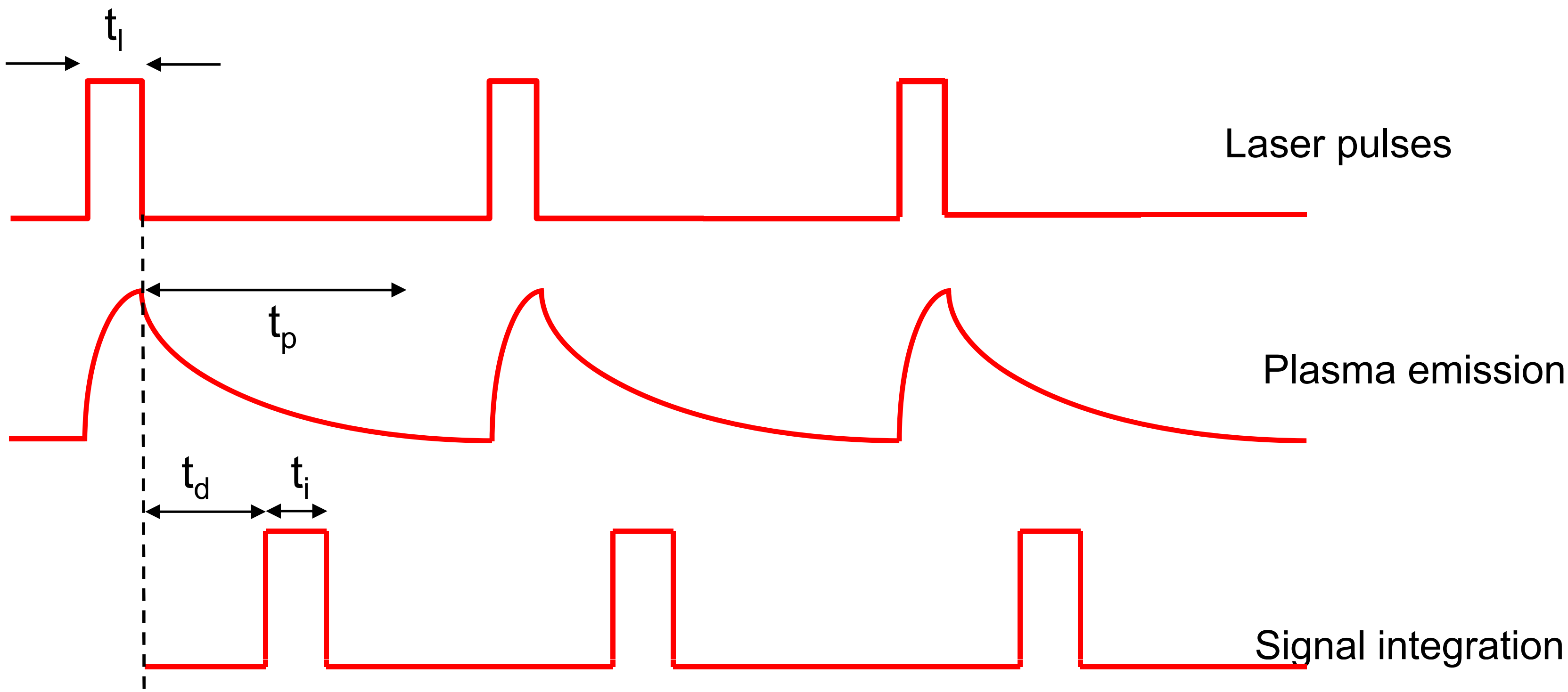

t_l : Temporal width of laser pulse
t_p : Plasma duration
t_d : Delay
t_i : Integration time

Laser Wavelength: 1064 nm

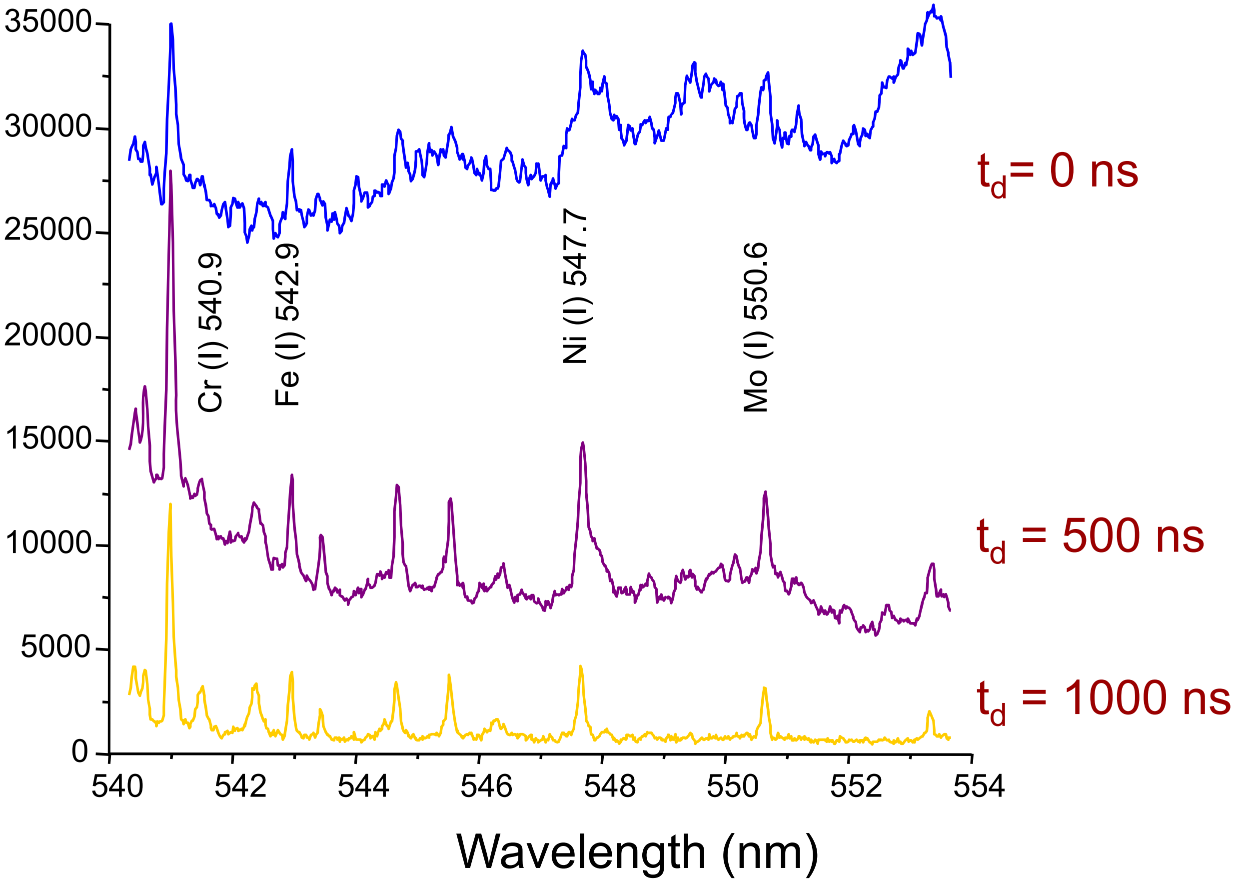

LIBS spectra

stainless steel

* 25 laser shots

* Integration time: 500 ns

Components and phenomena affecting LIBS analysis

Sample	Reflectivity, heat capacity, melting and boiling point, thermal conductivity etc.
Laser	Pulse energy, duration, spot size, wavelength
Plasma	Surrounding atmosphere (pressure, nature)
Spectrometer	Échelle spectrometer, Czerny-Turner, Rowland circle
Detector	IPDA, ICCD, Interline CCD, gated CCD, PMs

Mechanisms involved in the laser-material interaction

Laser-gas

Photon absorption and scattering•
Breakdown •
Plasma formation•
Laser-plasma interaction (inverse Bremsstrahlung,photoionization…)•
Shock wave formation•
Hydrodynamic expansion•
Unidentified mechanisms•

Laser-solid target

- Reflection (time dependent)
- Melting
- Vaporization
- Crater formation
- Stress wave in the target
- Plasma-material interaction (radiative heating, pressure)
- Ejection of solid fragments or ions target

4. Plasma spectral analysis

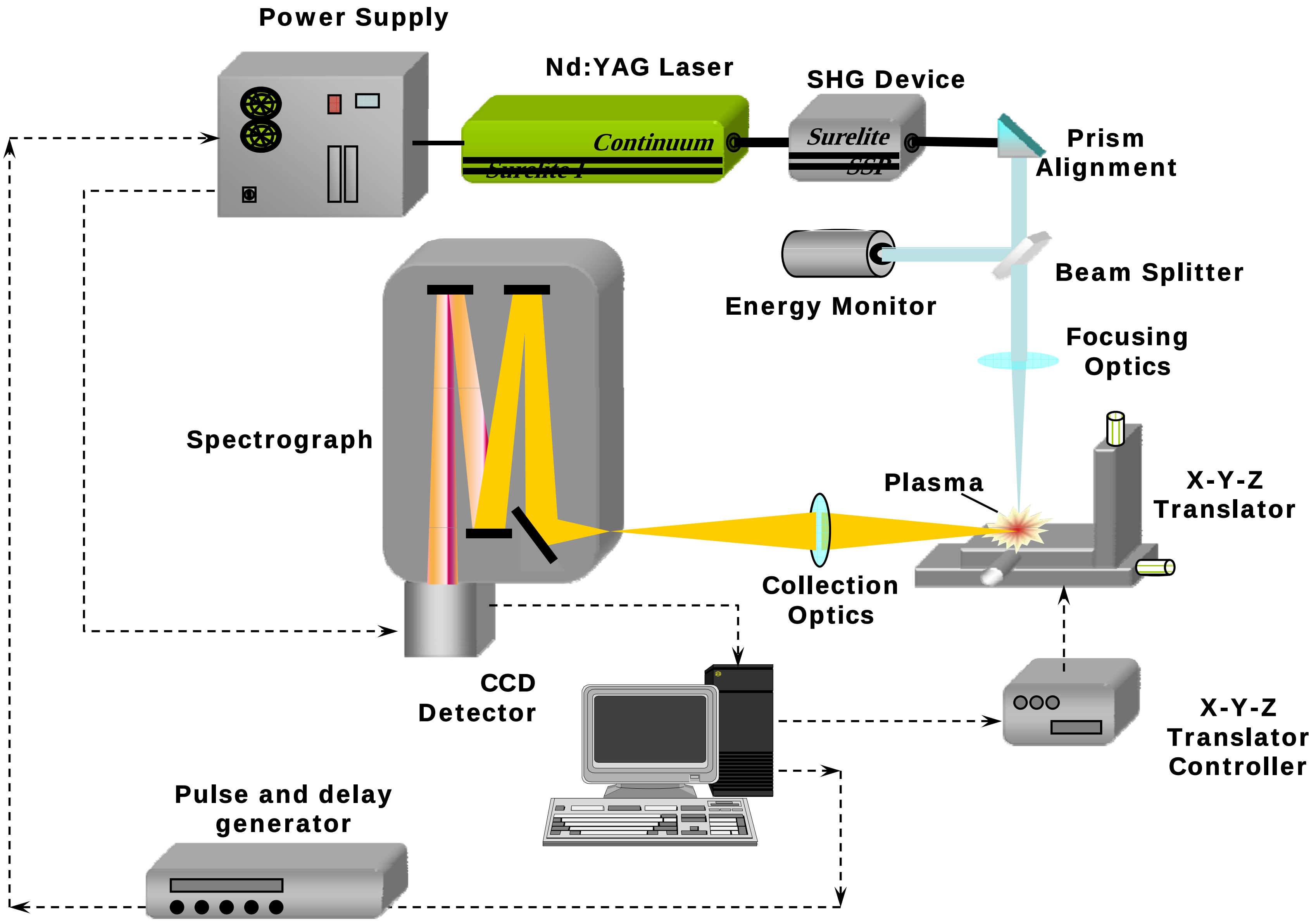

LIBS analysis capabilities

A large range of matrices can be studied by LIBS

SOLIDS

- Metals
- Ceramics
- Semiconductors
- Polymers
- Pharmaceuticals
- Teeth
- Soils
- Minerals
- Bacteria on agar substrate
- Metals immersed in water
- Wood, paper

Laser spark on a solid surface

LIQUIDS

- Molten metals, salts and glass
- Industrial effluents
- Process liquids
- Pharmaceutical preparations
- Biological fluids
- Water (Environment)
- Colloids

Laser spark on a liquid surface

GASES

- Industrial exhaust streams
- Combustion environments
- Aerosols in ambient air
- Proof-of-concept for detection of chemical warfare agents

Laser spark in a gas

LIBS advantages

- Applicable to every sample type
  - Solids
  - Liquids
  - Gases
  - Aerosols
  - Insulators/Conductors/Semiconductors
  - Refractory samples
  - Melted material
- Room temperature and atmospheric pressure operation
- Multielemental capability
- Sample preparation unnecessary
- Low sample requirements (ng-μg/pulse)
- Fast

LIBS drawbacks

- Detection limits (order of ppm)
- Precision and accuracy
- Some elements are hardly detectable (Cl, S, …)

Surface sensitivity: Beam focal conditions

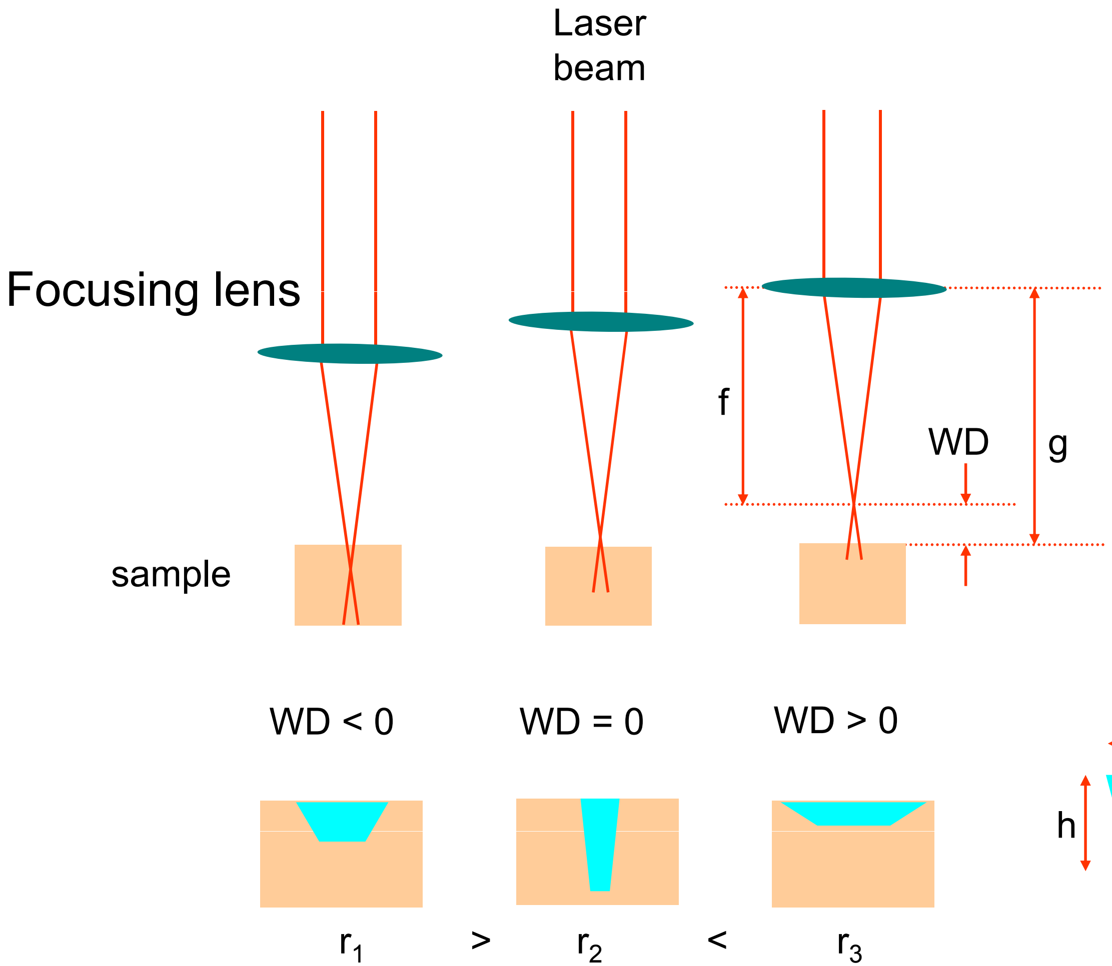

WD working distance

f lens focal length

g lens-to-sample distance

$$WD = g - f$$

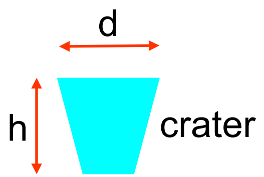

Aspect ratio $r = d/h$

Detection of surface impurities on monocrystalline silicon

Nd:YAG Laser @ 532 nm, 5 mJ pulse^{-1}

WD = - 5 mm

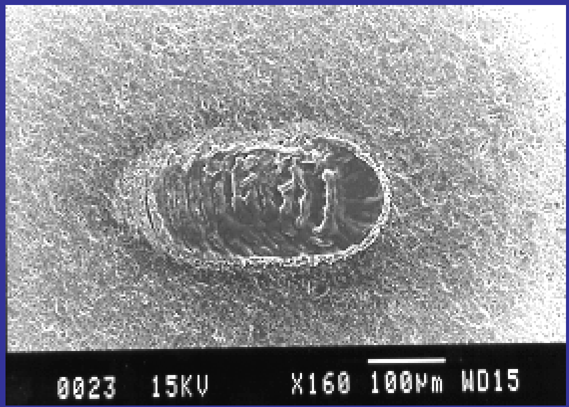

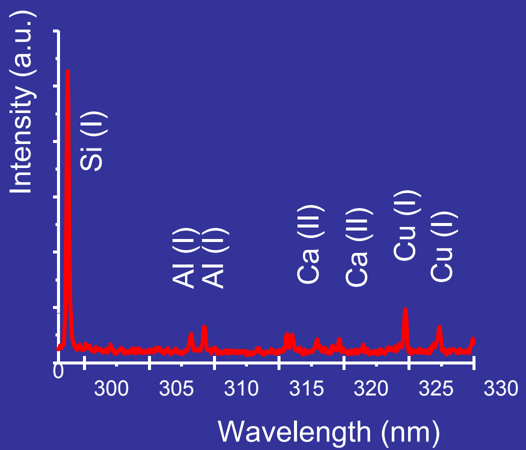

WD = 0 mm

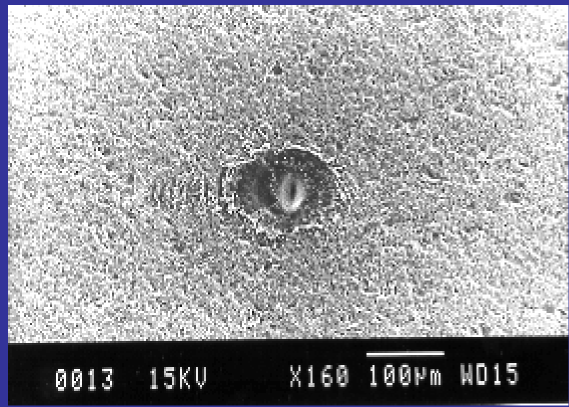

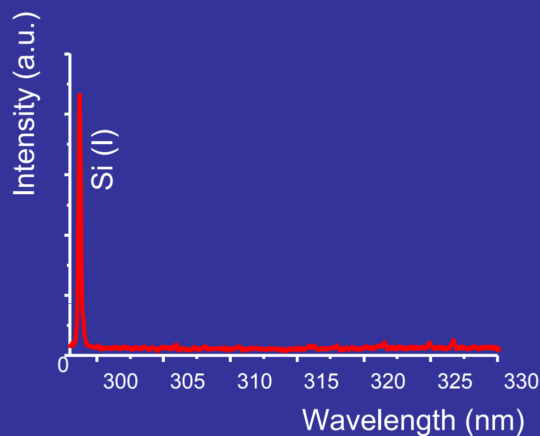

WD = + 5 mm

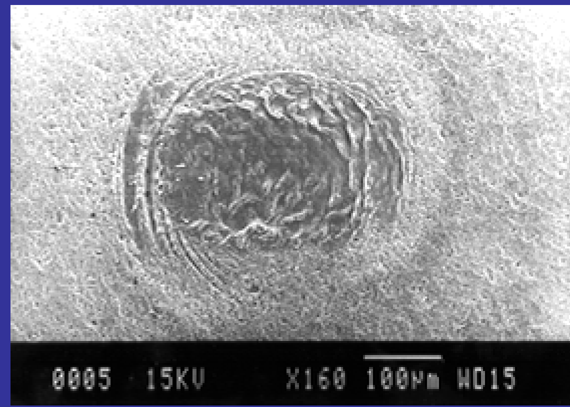

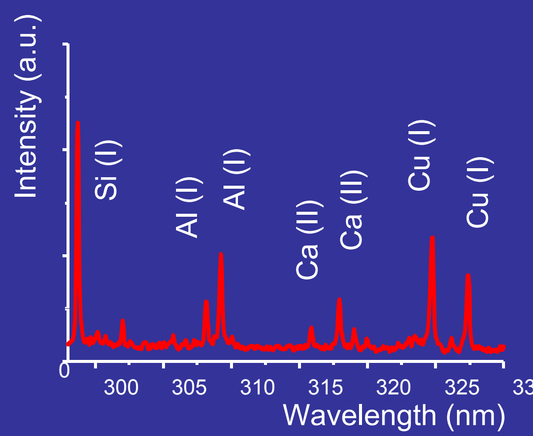

Single-shot spectra

Surface sensitivity : effect of pulse energy

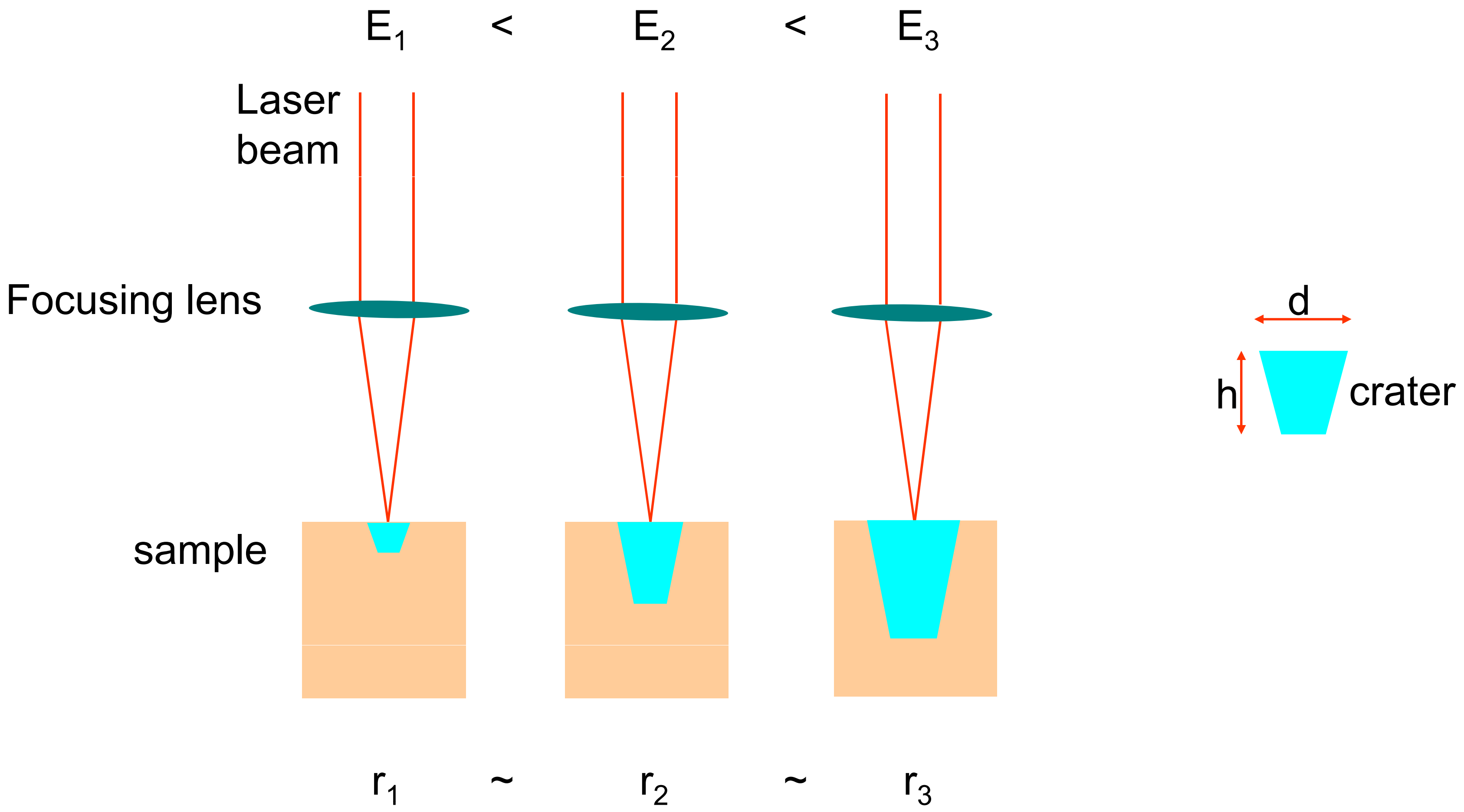

Effect of pulse energy

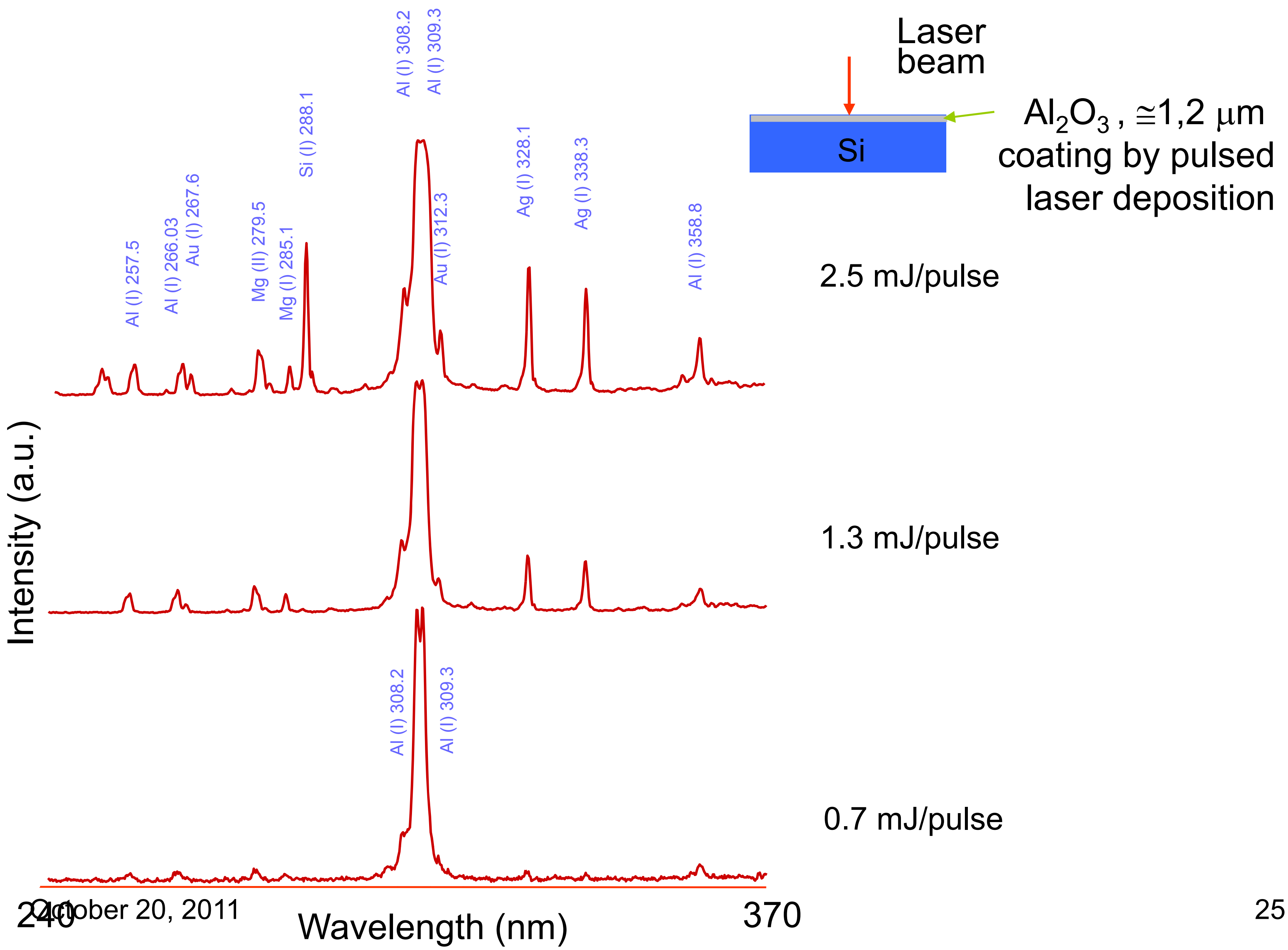

Design and construction of Q-Switched Nd: YAG Laser System for LIBS Measurements

❑ The aim of this work is to design and build Nd:YAG laser system to meet the following requirements:

i. Able to deliver peak power greater than that needed for breakdown threshold.
ii. Multi-pulse laser source since multi-pulse laser system enhance the signal intensities.
iii. Provide a potential compact, robust laser source for portable LIBS system.

❑ A single passive laser shot contains train of pulses is required. Each pulse should be in the range of 1 MW/cm^2. Assuming the pulse width of the passive Q-switch is in the range of nanoseconds, and the energy of each pulse is about or more than 25mJ; the total Q-switched energy of each shot should be in the range of 100-170 mJ

The Overall System Block Diagram

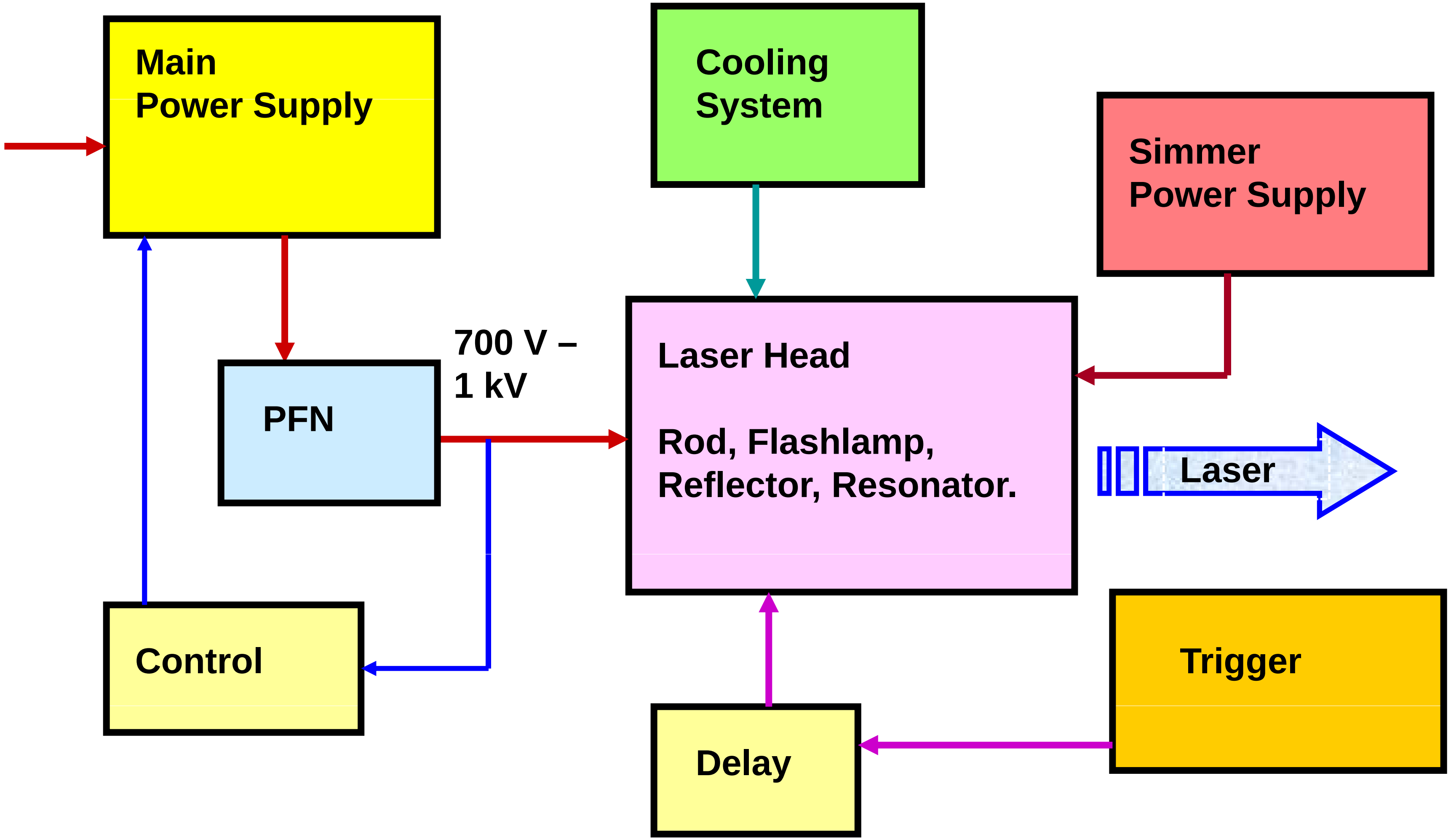

Laser Resonator

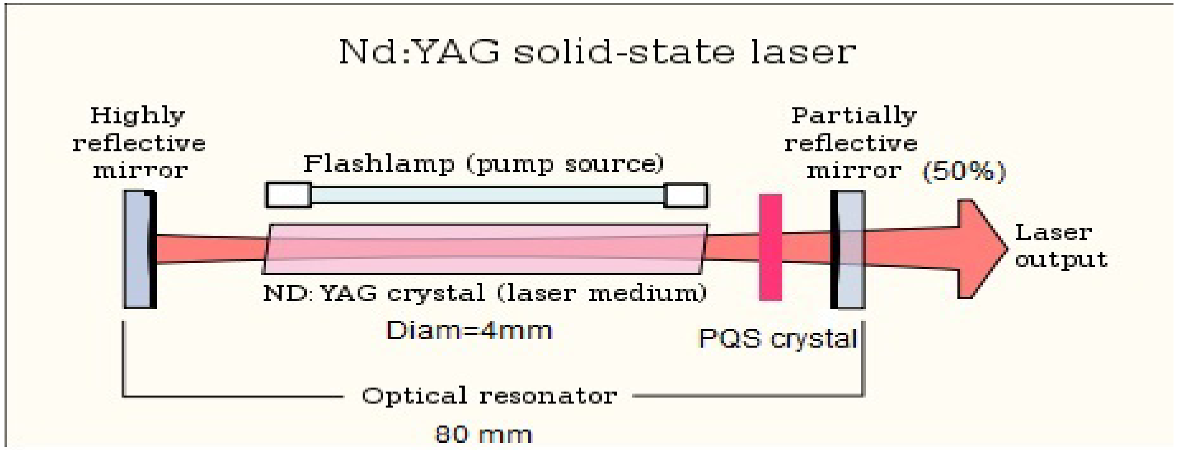

The selection of the cavity configuration depends upon the following three factors

- diffraction loss,
- mode volume and
- ease of alignment.
- The plane parallel cavity configuration is very useful for pulsed solid state lasers
  - large mode volume,
  - no focusing inside the laser cavity.
  - Disadvantage: diffraction losses can be easily overcome by high laser medium gain. .

Pump cavity

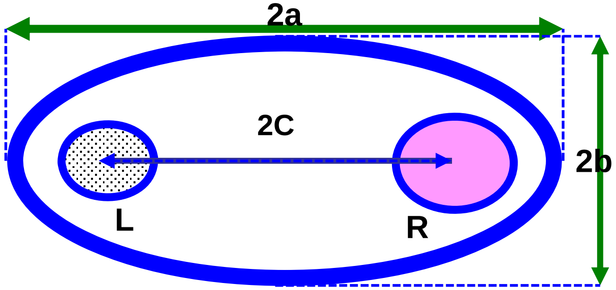

$r_r / r_L = 1.2$

$C = (a^2 - b^2)^{1/2}$,

$e = C/a$

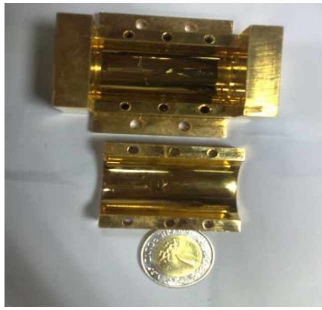

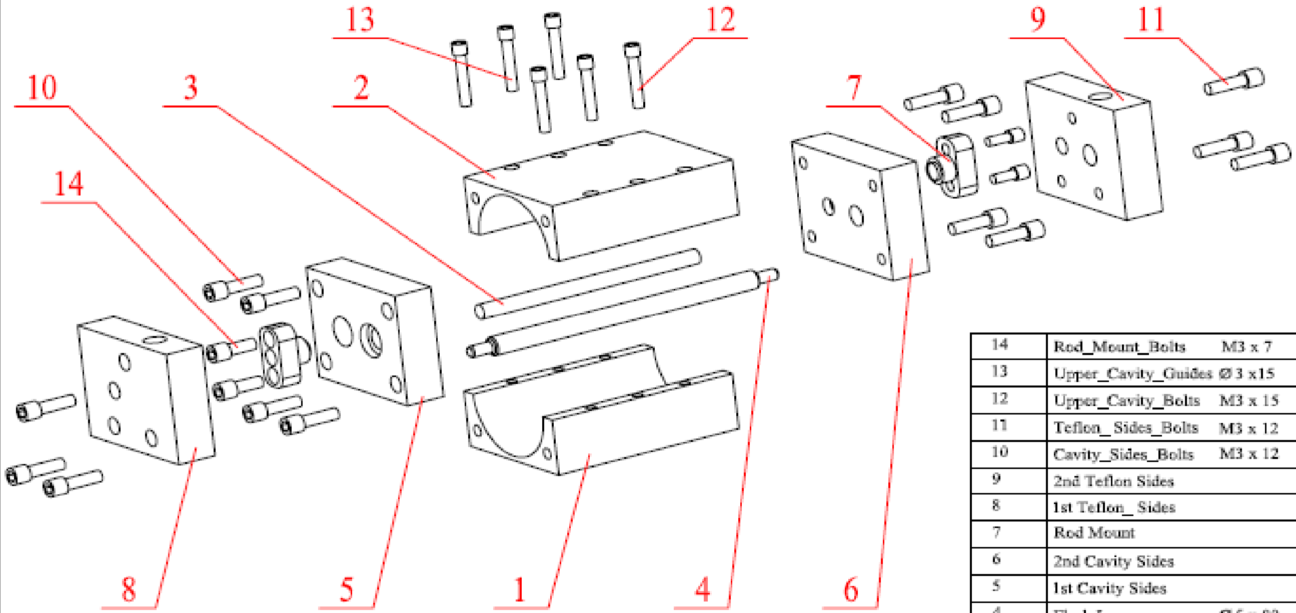

14	Rod_Mount_Bolts	M3 x 7	4
13	Upper_Cavity_Guides	Ø 3 x15	2
12	Upper_Cavity_Bolts	M3 x 15	4
11	Teflon_ Sides_Bolts	M3 x 12	6
10	Cavity_Sides_Bolts	M3 x 12	8
9	2nd Teflon Sides		1
8	1st Teflon_ Sides		1
7	Rod Mount		2
6	2nd Cavity Sides		1
5	1st Cavity Sides		1
4	Flash Lamp	Ø 5 x 80	1
3	Rod	Ø 4 x 60	1
2	Pump Cavity Upper Part		1
1	Pump Cavity Lower Part		1
NO.	NAME		QUNTITY

Project : Pulsed ND:YAG Laser System		
General Tolerance 0.05 mm	Material	Sh: of:
Design	Denomination Cavity Disassembly of pulsed ND:YAG Laser System	Scale
Check		

Driving circuit of flashlamp

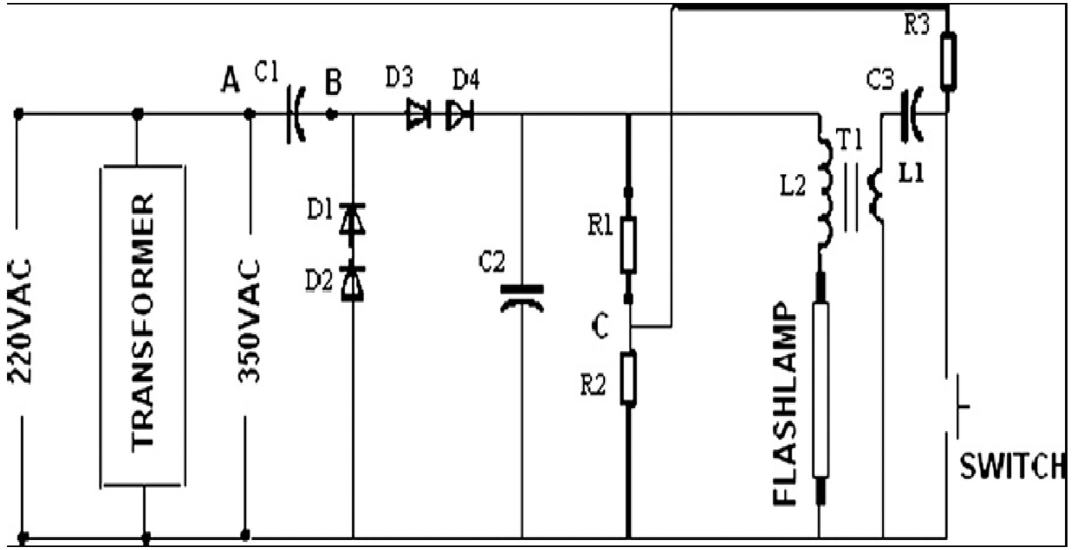

Component	Value
C1	0.2µF/600v
C2	101µF/2.0kv
L2	99µH (60 turns) Øw2 = 1.5mm
L1	(3 turns) Øw1 = 1.5mm
D1-D4	1N5408
C3	0.47 µF /600V
R1,R2	150 kΩ/1W
R3	10 kΩ/1W

Laser Characteristics

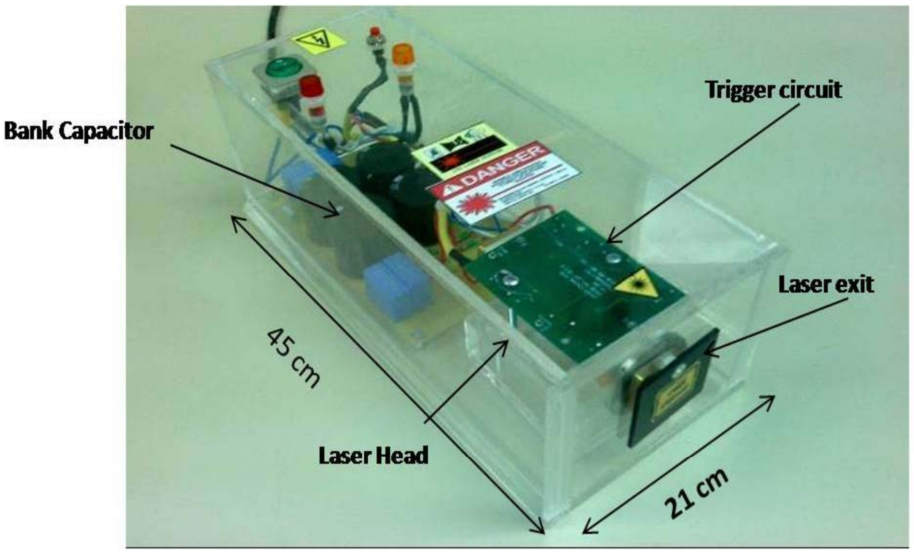

Real photo of the Nd:YAG laser system

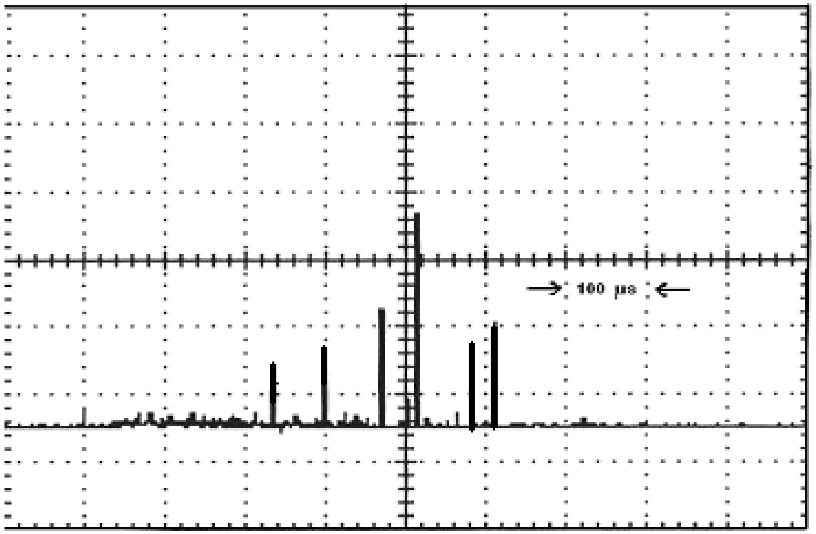

Temporal profile of passively Q-switched laser pulses

System validation

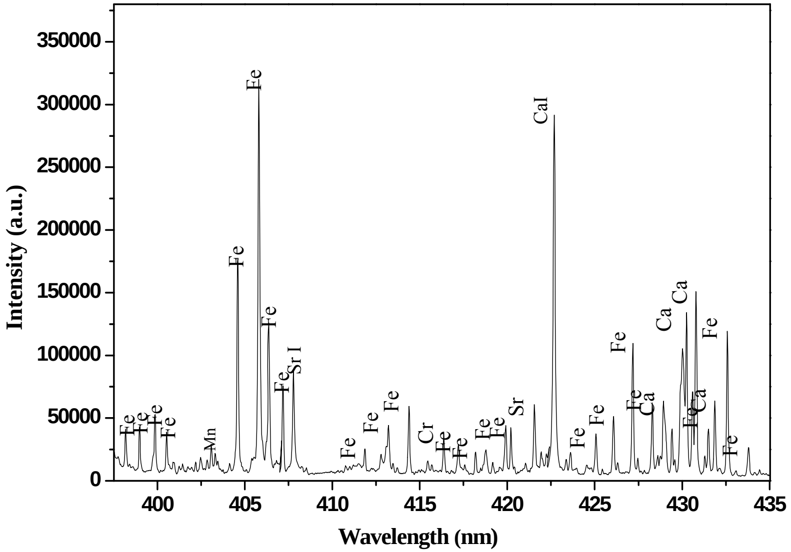

Emission spectra from mamlouki brown ceramic body of archaeological samples

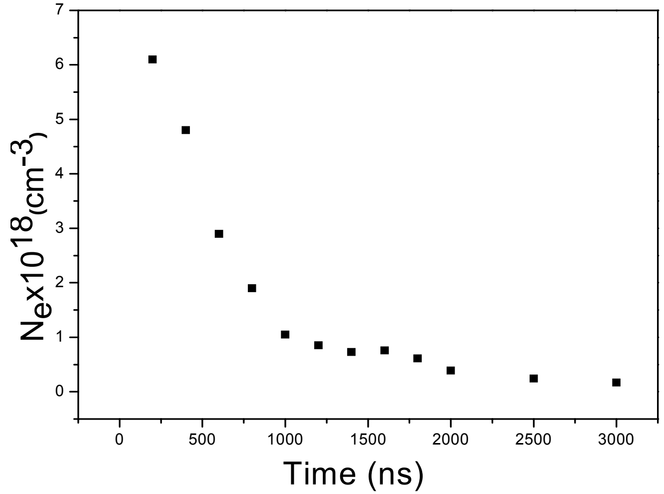

Electron density temporal evolution (Ne)

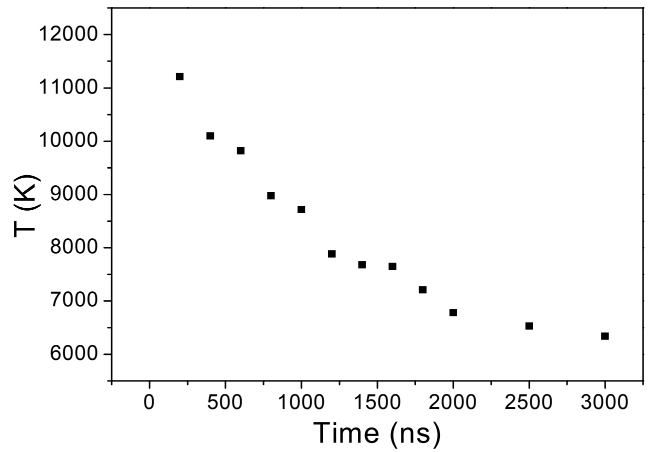

Temporal behaviour of the plasma temperature obtained via Boltzmann equation

Conclusion

- Multipulse passive Q-switched Nd: YAG laser system has been designed and build.
- To validate the the laser system, it was used in LIBS experiment

Assessment of LIBS diagnostics of plasma using the hydrogen H_α- line at different laser energies

- Assess the measurements of the laser produced plasma electron density using the hydrogen H_α-line at 656.27 nm associated with the emitted spectra from aluminium target at different laser energy in the range from 175 up to 600 mJ.

- H_α-line at 656.27 nm is well isolated, survive for longer times, has relatively large FWHM, and self absorption free

Experimental Setup

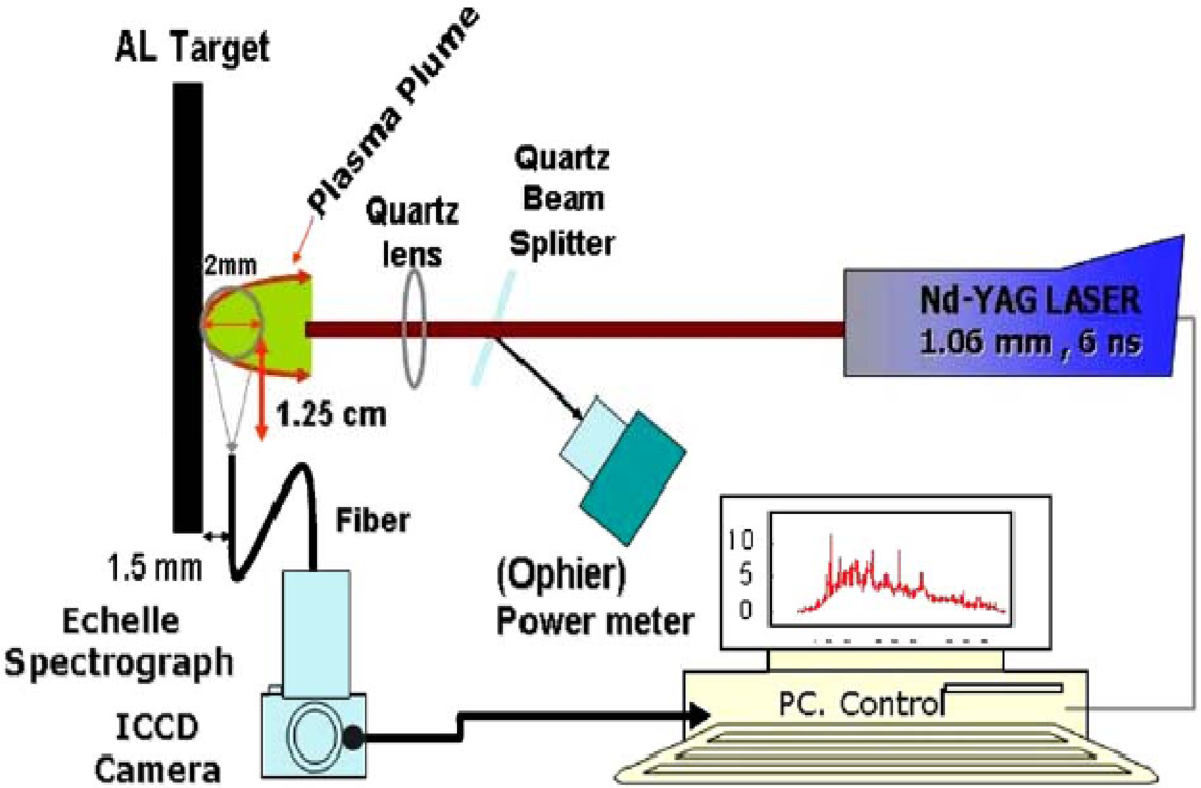

Fig. 1. Experimental set-up.

Results

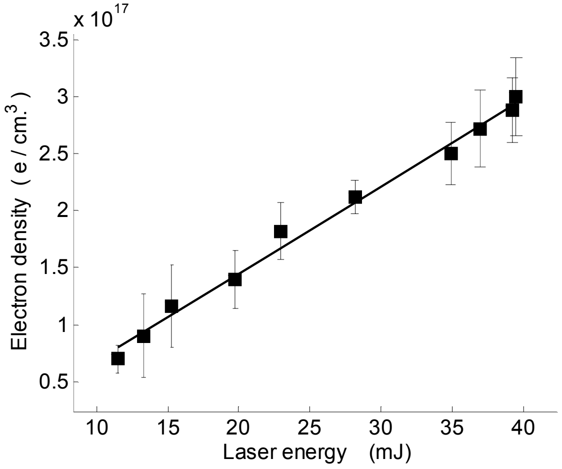

The variation of the measured electron density utilizing the H_a line with the laser energy

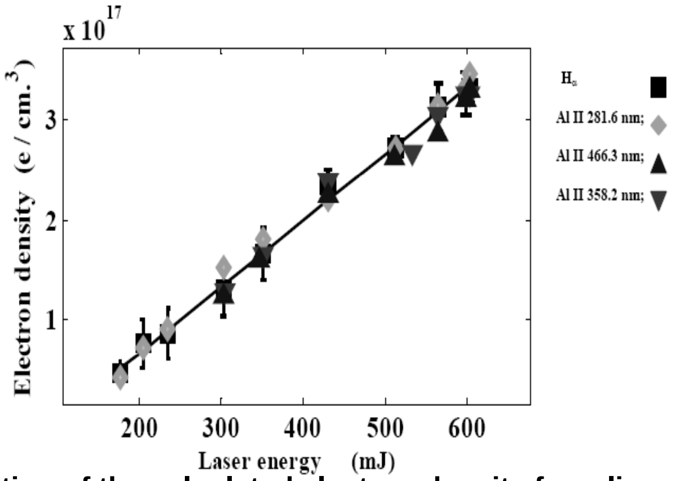

The variation of the calculated electron density from lines of the Al II with laser energy in comparison with the values from the H_a line

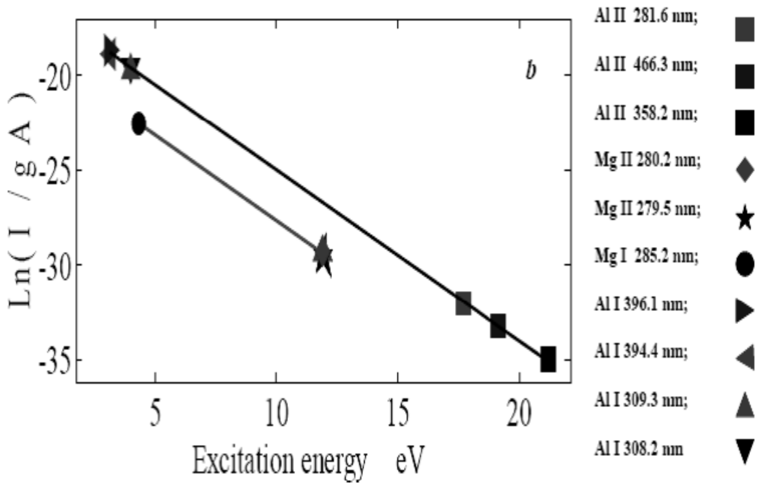

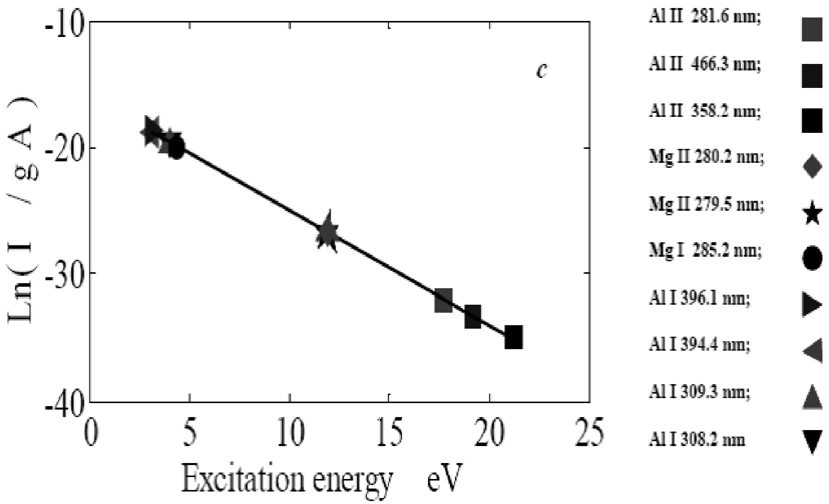

(a) Multi-line Saha-Boltzmann plots after correction of Al I and Mg I, II lines against self absorption (Upper and lower solid lines, respectively). (b) Multi-elemental Saha-Boltzmann plot after correcting the Mg lines by their relative concentration.

The overall variation of the calculated electron temperature utilizing the multi-elemental Saha-Boltzmann plot after correction of spectral lines against self absorption with the laser energy

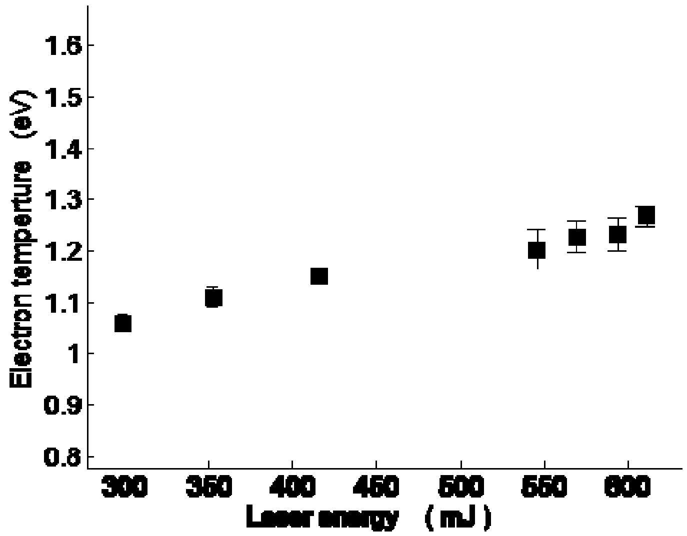

Conclusion

➤The electron density of the plasma was measured by using the H_α-line and the Al lines as well as from Mg lines in the range of laser energy from 170 to 600 mJ under the same conditions.

➤Linear increase in the electron density was found. In contrast to Al I and Mg I, II lines, the spectral lines of Al II were found to be self absorption free. This may be attributed to the large concentration of atoms in the ground state of the inherent resonance transitions.

➤A correction to the lines intensities at the central emitted wavelength was done utilizing the ratio of the electron densities from the different lines to that measured from the H_a-line. A compatible Saha-Boltzmann plot of the spectral line intensities could be obtained only after correction of self absorption effect, which turned out to be crucial in any reliable characterization of plasma

Experimental investigation of double pulse laser induced plasma spectroscopy in bulk water

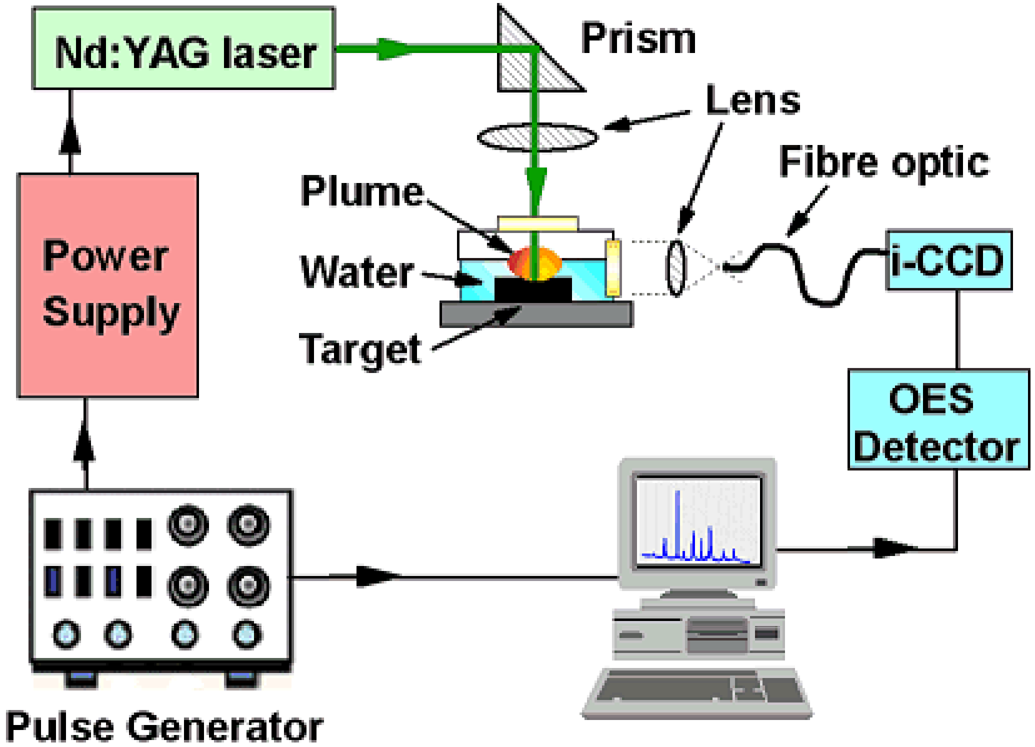

Double pulse laser induced plasma spectroscopy in bulk water

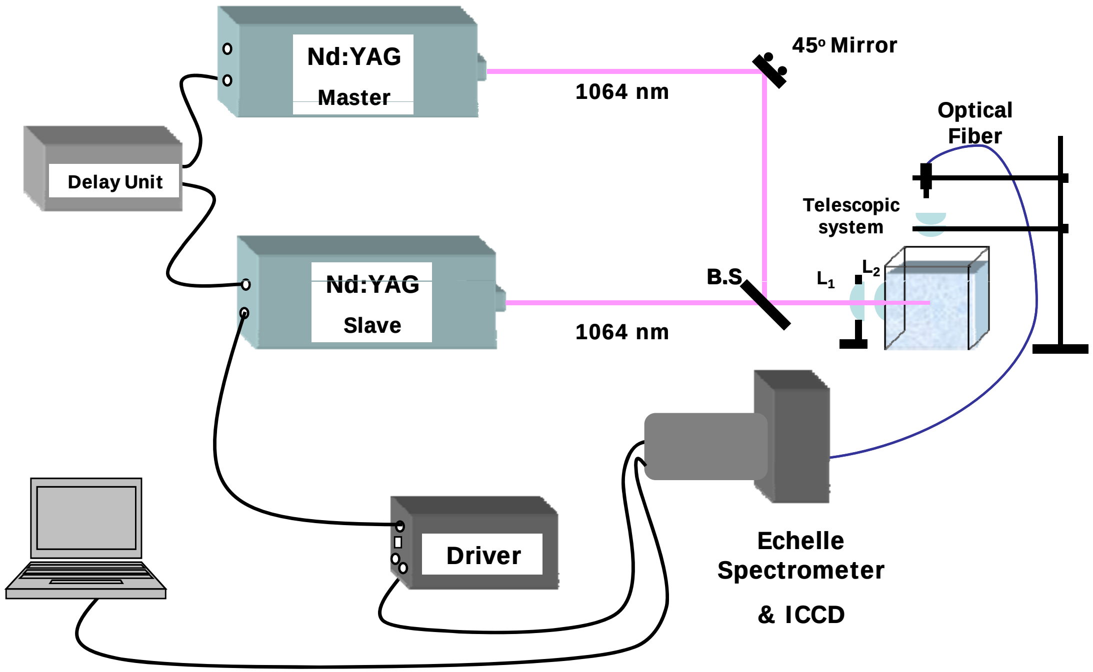

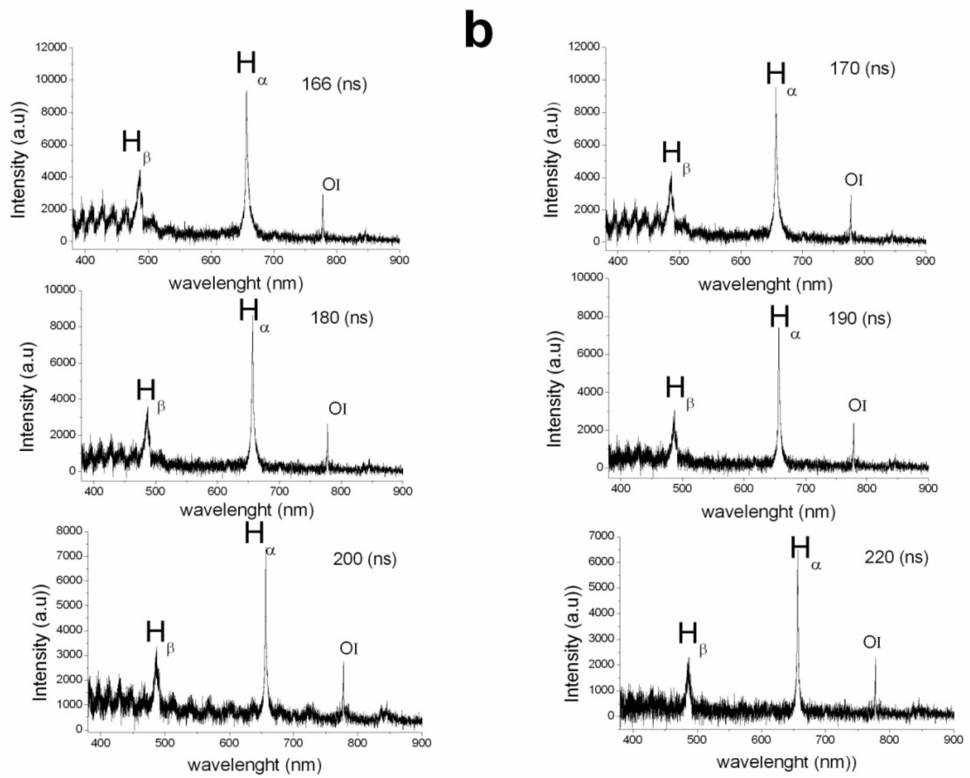

Temporal evolution of plasma spectra at gate width 10 μs as a function of (a) inter-pulse delay at gate delay 166 ns, and (b) gate delay at inetr-pulse delay 30 μs.

Combustion Projects

"**Detailed Studies of Premixed and Partially Premixed Burners Using Highly Advanced Laser-Based Techniques**"
Combustion Division, Lund University, Lund - Sweden
31/12/2009 – 2006
(SIDA) Swedish International Development Agency – Sweden

"**Computational and Experimental Studies of the Structure and Dynamics of Premixed Flame Kernels under Turbulent Conditions**"
North Carolina State University, North Carolina, USA
Prof. Tarek Echekiki, North Carolina State University
31/12/2011 – 2009
US-Egypt funding - STDF

Local equivalence ratio measurements in turbulent partially premixed flames using laser-induced breakdown spectroscopy

- The aim of this work is to study the application of the double pulse LIBS technique for turbulent flame measurements. The technique is applied to two turbulent natural gas partially premixed flame stabilized by conical nozzle.

- Quantitative measurements of the elemental mass fractions and equivalent ratio.

- Equivalence ratio, ϕ, which is defined as the ratio between the stoichiometric air-to-fuel ratio and the actual air-to-fuel ratio. So, at $\phi = 1$ the mixture is stoichiometric, i.e. the air is just enough to burn the fuel, while for $\phi < 1$ the mixture is lean, i.e. excess air, and for f > 1 the mixture is rich, i.e. excess fuel.

- Equivalent ratio and mixture fraction are important parameters used in combustion models to understand the combustion process and to describe and predict flame.

Experimental Setup

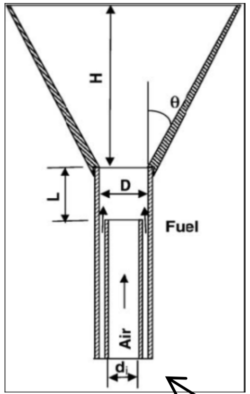

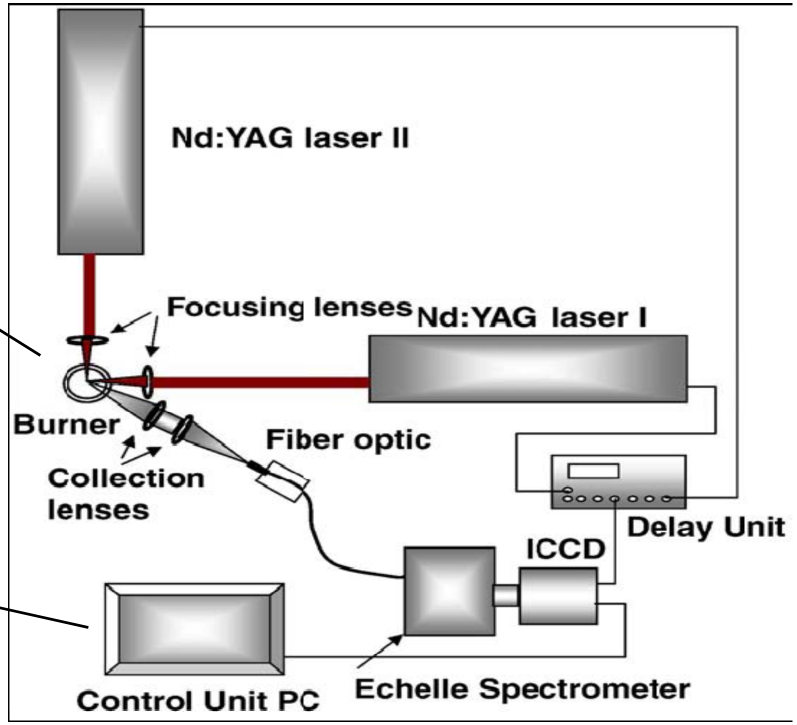

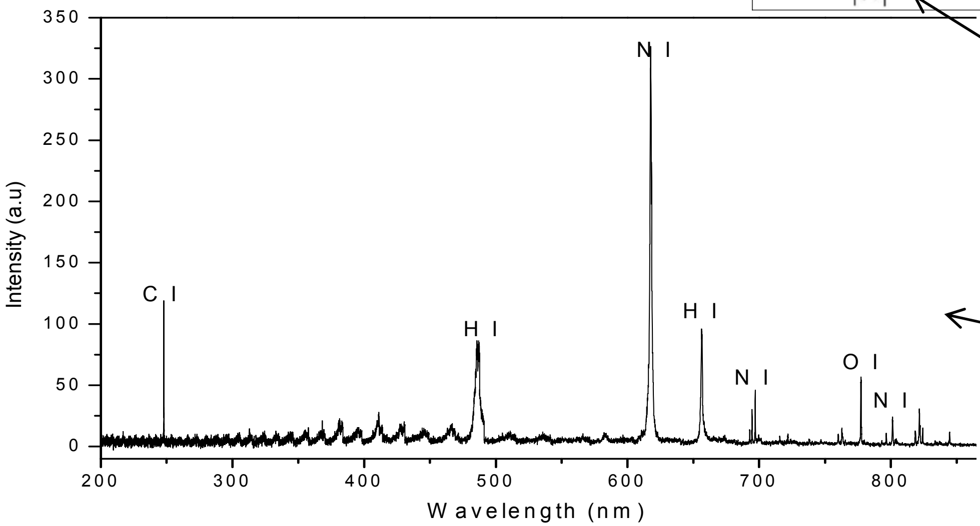

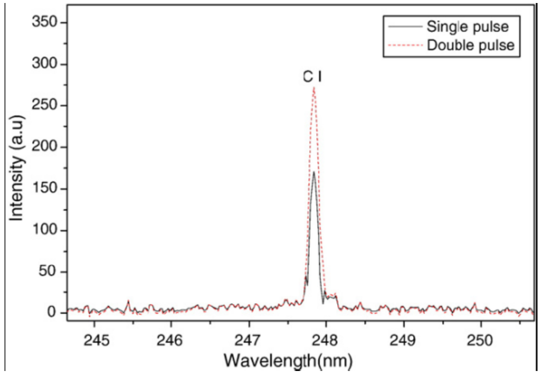

E=100mJ, pulse width 8ns
Delay between two pulses=250ns
Gate width 10000ns, Gate delay = 1000ns from the 2nd laser

Results

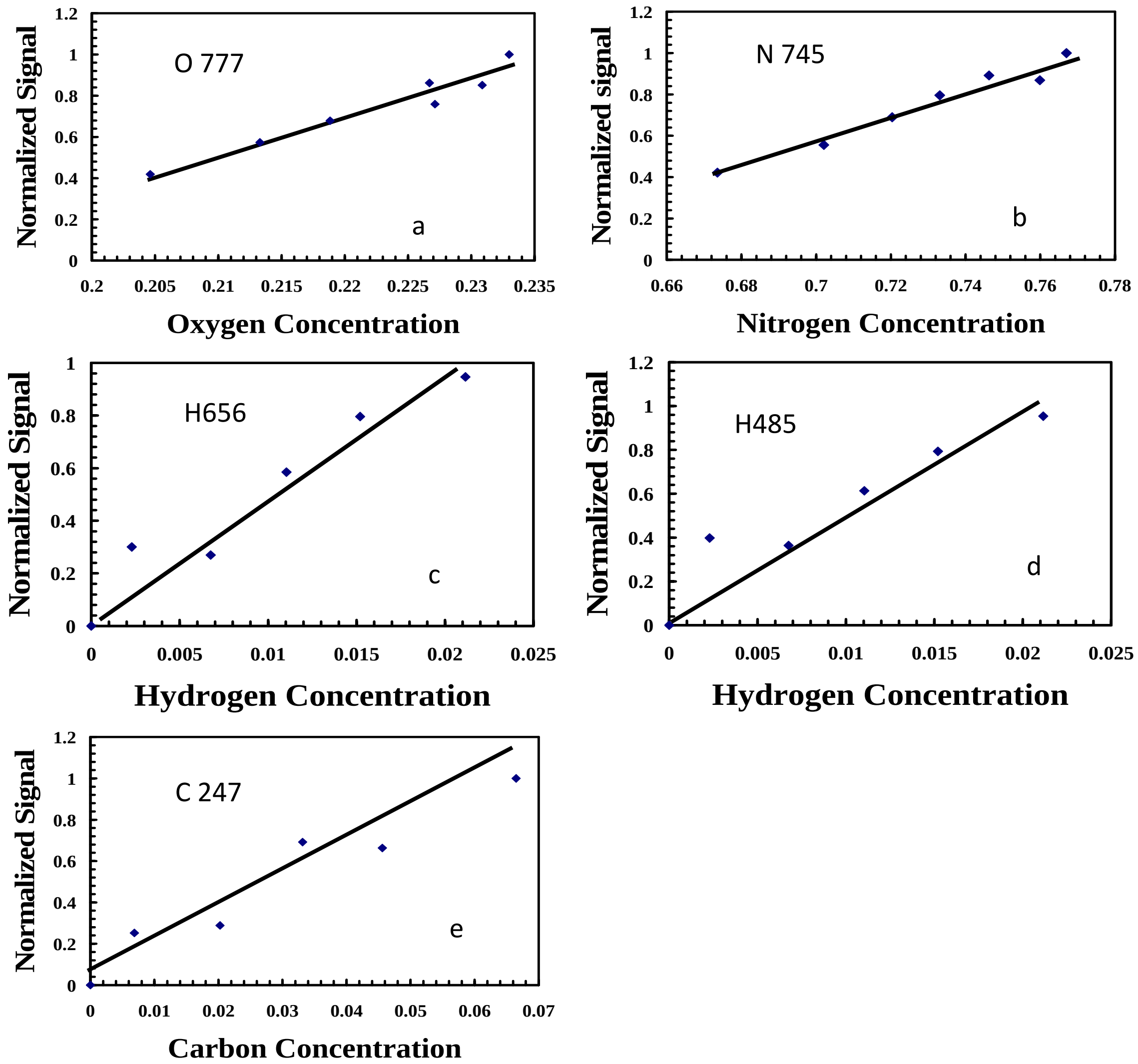

The calibration curves for the lines (a) O at 777 nm, (b) N at 745 nm, (c) H at 656 nm, (d) H at 485 nm and (e) C at 247 nm.

Flam Measurements

The mixture fraction, ξ,

$$\xi = \frac{\varphi}{\varphi + \left(\frac{A}{F}\right)_{st}}$$

where $(A/F)_{st}$ is the stoichiometric air-to-fuel ratio and is equal to 17.167 in the present flames with natural gas

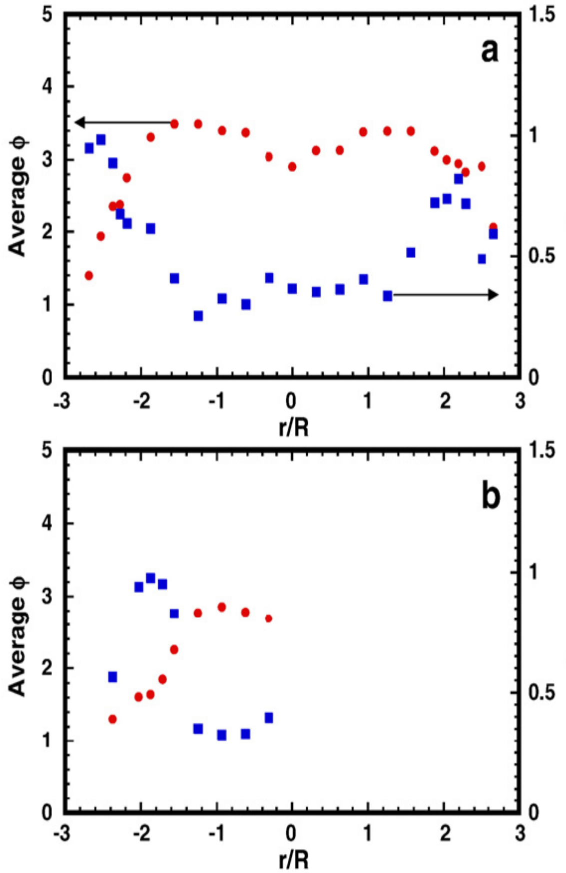

Figure 8 Radial profiles of the average and rms of the equivalence ratio in both flames at (a) ϕ = 3 and (b) ϕ = 4

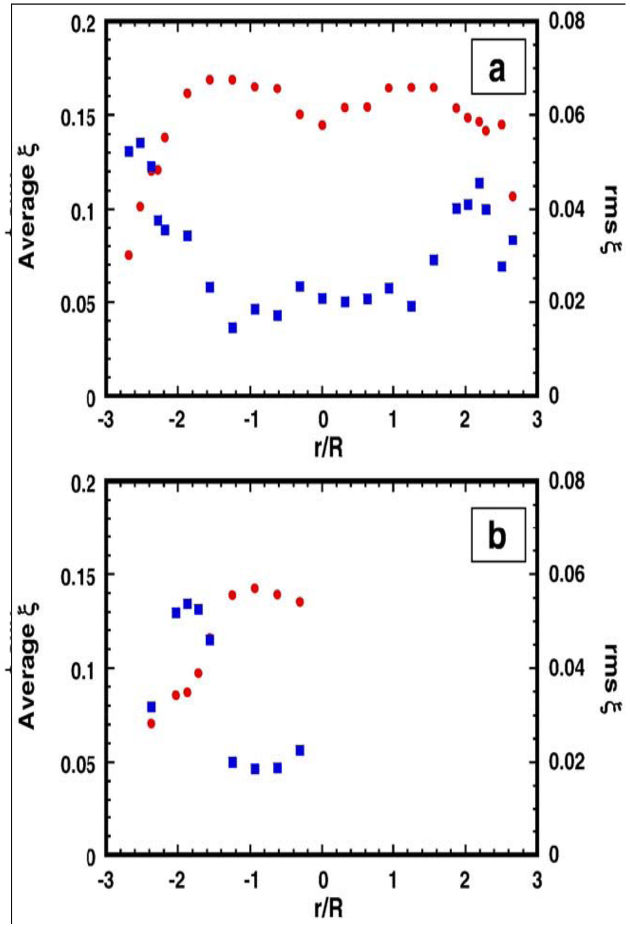

Figure 9 Radial profiles of the average and rms of the mixture fraction in both flames at (a) ϕ = 3 and (b) ϕ = 4

Conclusion

- LIBS technique is able to measure the local equivalence ratio in turbulent environment from single shot with double pulse laser.

Laser-Induced Breakdown Spectroscopy Technique in Identification of Ancient Ceramics Bodies and Glazes

- The aim of this work is to use Laser Induced Breakdown Spectroscopy (LIBS) as a promising non-destructive technique for the identification of the colored glazes, and clay's bodies of Fatimid ceramics ancient artifacts.

- The scientific examination of ceramics may be helpful in unravelling the history of ancient shards, particularly as the process of its production such as firing condition and temperatures.

- The analysis of pottery, ceramic bodies and glazed coatings is required in order to structure the conservation or restoration of a piece.

Experimental Setup

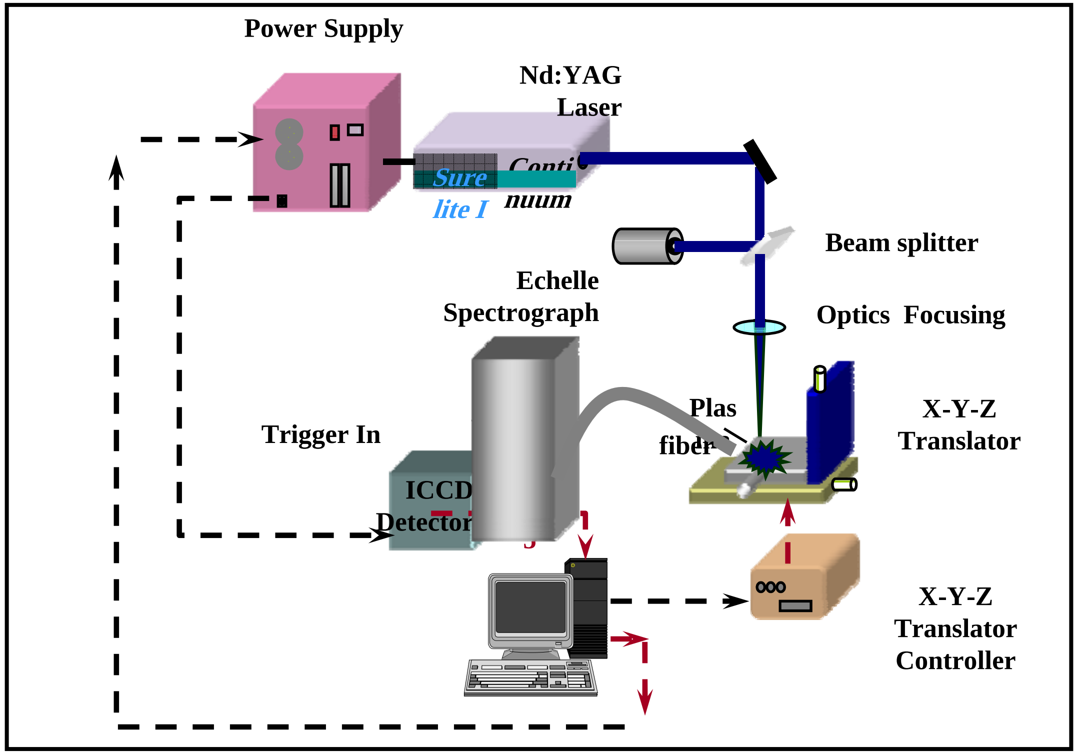

samples

Results

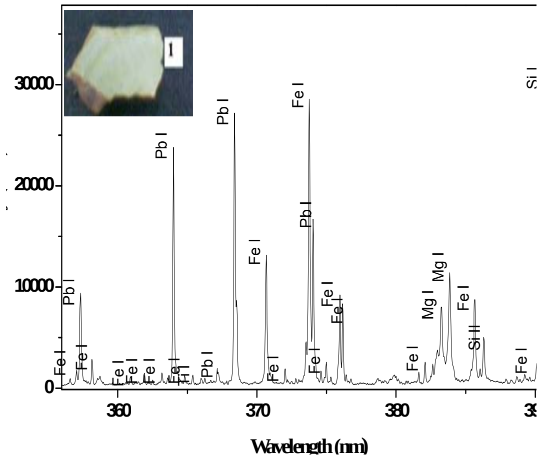

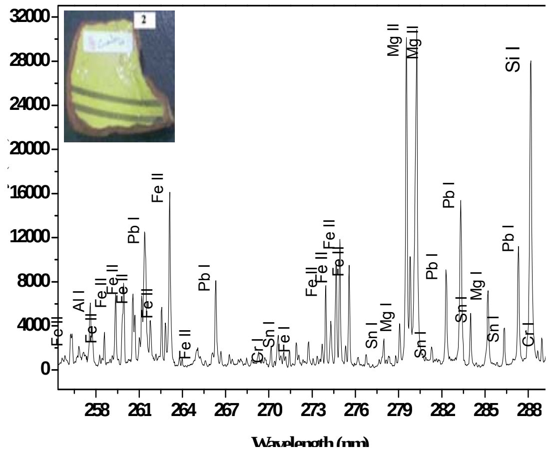

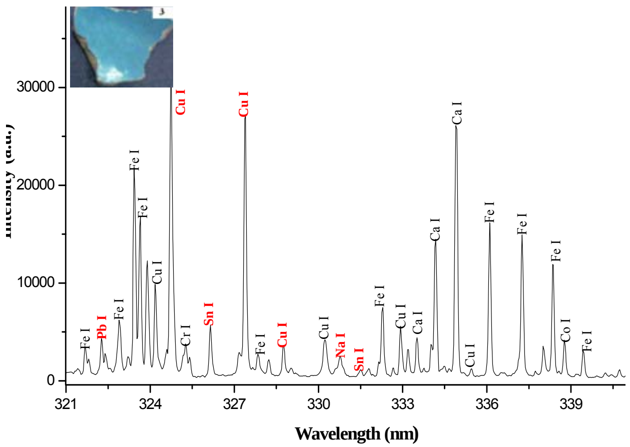

LIBS spectrum of glaze sample no 1,2,3

Conclusion

- The information extracted from LIBS results suggested that LIBS can be employed to determine/confirm the date of certain types of pottery.

- The scientific examination of ceramics may be helpful in unravelling the history of ancient shards, particularly as the process of its production such as firing condition and temperatures.

- The analysis of pottery, ceramic bodies and glazed coatings is required in order to structure the conservation or restoration of a piece..

A comparative study of laser cleaning of archaeological inorganic materials with traditional methods

Samples description

- All samples were excavated from El-Fustat excavation in Old Cairo.
- El-Fustat founded as a first capital of Islamic Egypt (21AH / 641 AD).
- The samples may be belong to Abbasid period (132 AH / 750 AD).
- The samples collected were glass, pottery and bronze contaminated with different deposits

Al-Fustat Location (East Nile)

Laser Cleaning (Pottery sample)

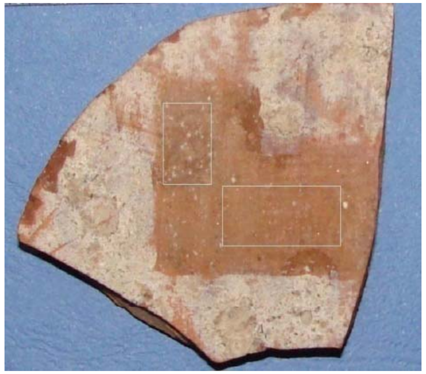

area of pottery sample no.1
after cleaning by laser with

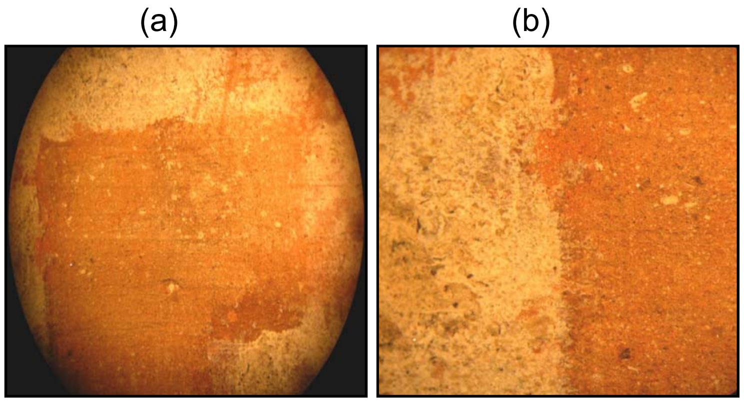

Fig. (a-b) Shows the area of pottery sample no.1 after cleaning by laser (magni.12 X- 25 X)

Traditional cleaning (Pottery sample)

he area of pottery sample no. 1
after cleaning by

(a) (b)

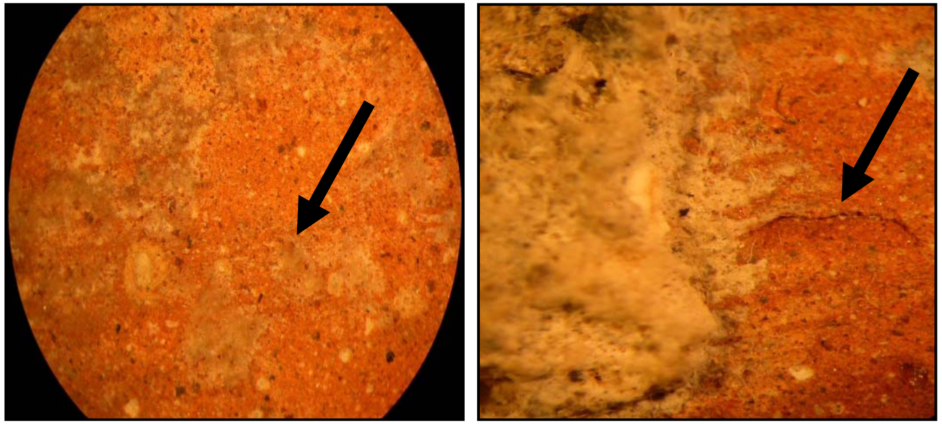

Figs.(a-b) Shows staining and erosion in surface of pottery sample no.1 after cleaninbg with chemicals

Comparative study of laser cleaning and traditional cleaning (Pottery sample)

(a) (b)

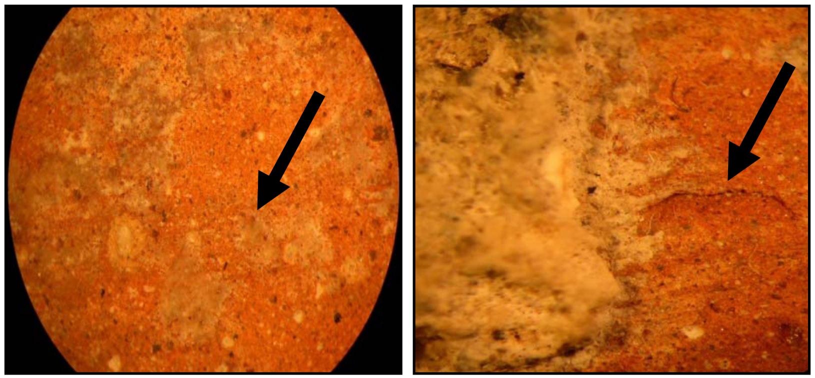

Figs.(16 a-b) Shows staining and erosion in surface of pottery sample no.1 after cleaninbg with chemicals

(a) (b)

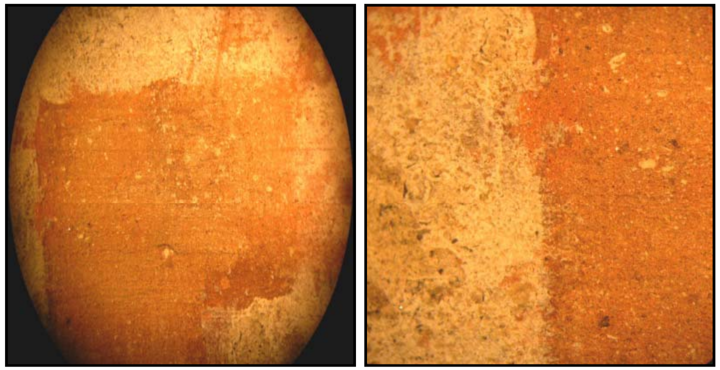

Fig. (a-b) Shows the area of pottery sample no.1 after cleaning by laser (magni.12 X- 25 X)

Laser Cleaning (Pottery sample)

Fig Shows the area of pottery sample no 2 after cleaning by laser

(a) (b)

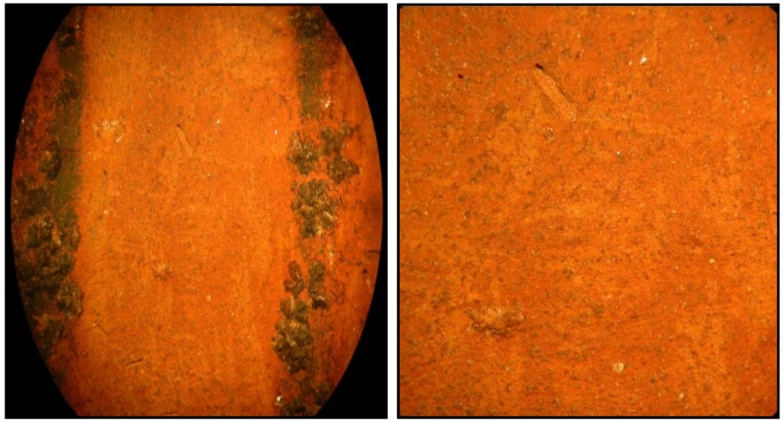

Figs.(a-b) Shows the surface of pottery sample no.2 after cleaning by laser with magni. 12X- 50X

The impact of the telescope selection and diaphragm design in LIDAR signal-to-noise ratio improvements

- **Elimination of background noise in the daytime measurements** in case where full overlap between laser beam and receiver telescope field of view is necessary.
- Range and sensitivities of lidar measurements in daylight are limited bysky background noise (BGS)
- Raman lidar signal is relatively weak, this often restricts Raman lidar measurements to nighttime where BGS is absent
- Significant improvements in Lidar signal to noise ratio (SNR) and attainable lidar ranges can be obtained, by minimizing the detected sky BGS which dominates all the other forms of noise
- **a diaphragm design and the receiver telescope proper parameters selection can reduce the detected sky background noise**.
- With moving the diaphragm position and select the proper telescope F# and field-of-view (FOV), the sky noise reaching the detector is minimized.
- Results show as much as a factor of 200% improvement in signal-to-noise ratio, as well as the corresponding range improvement.

Lidar equation:

$$P(\lambda_L, R) = P_L \frac{A_o}{R^2} \xi(\lambda_L) \beta(\lambda_L, R) \xi(R) \frac{c\tau_L}{2} \exp\left(-2 \int_0^R k(\lambda_L, R)\, dR \right)$$

Where, P is the total scatter laser power received from a distance *R*, P_L represents the average power in the laser pulse, A_o/R^2 describes the solid angle of the receiver optics (A_o is the area of the telescope primary mirror), ξ(λL) denotes the receiver's spectral transmitter factor, β is the volume backscatter coefficient, cτ represents laser pulse length (*c* is speed of light, τ is Laser pulse rectangular duration), k: Atmospheric extinction coefficient. The smaller the value of ξ(R) is the smaller the return signal and the smaller SNR particularly for short distances. GF can be defined as the ratio of the energy transferred to the photodetector to the energy reaching the telescope primary mirror, E_{det} / E_{scat} [6].

Geometric Factor in Monostatic Biaxial Lidar

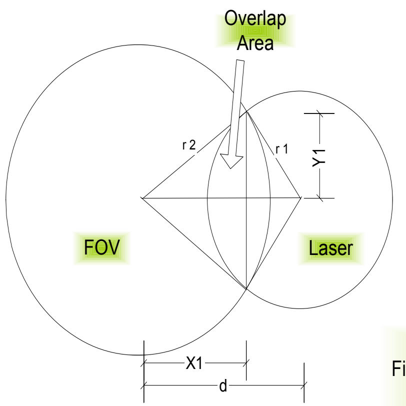

Fig. 1. Overlap Area Calculations

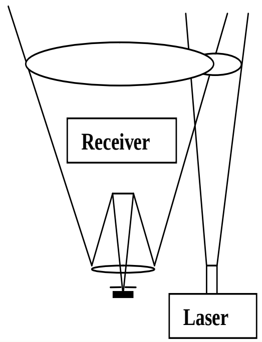

Fig. 2. Schematic diagram of elastic Biaxial Lidar Showing overlapping between field of view of receiver telescope and laser beam

The range 'R' increases, there will be a point 'R_o' where the first intersection between the laser beam and the telescope FOV, then partial overlap, and finally complete overlap

The image displacement is according to the distance 'L' between the laser and telescope optical axis and the altitude 'R'.

Lidar specifications used in the simulation

d = 0

L = 200 mm

W_o = 5 mm

r_0 = 177.8 mm

Θ = 0.7 mrad

f = 1000-4000 mm

R_{min} = 0.5 km

R_{max} = 25 km

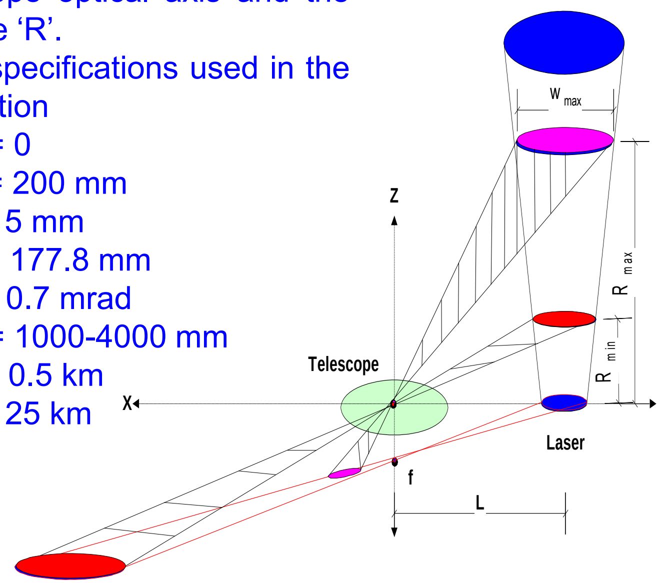

Minimizing the detected BGP using GF

Overlapping area /image area formed near f

$$\xi(R) = \frac{OL_{area}}{\mathrm{Im}_{area}} = 0$$

where $OL_{area} = 0$ effective telescope area $A_{eff}(R) = A_o\xi(R) = 0$

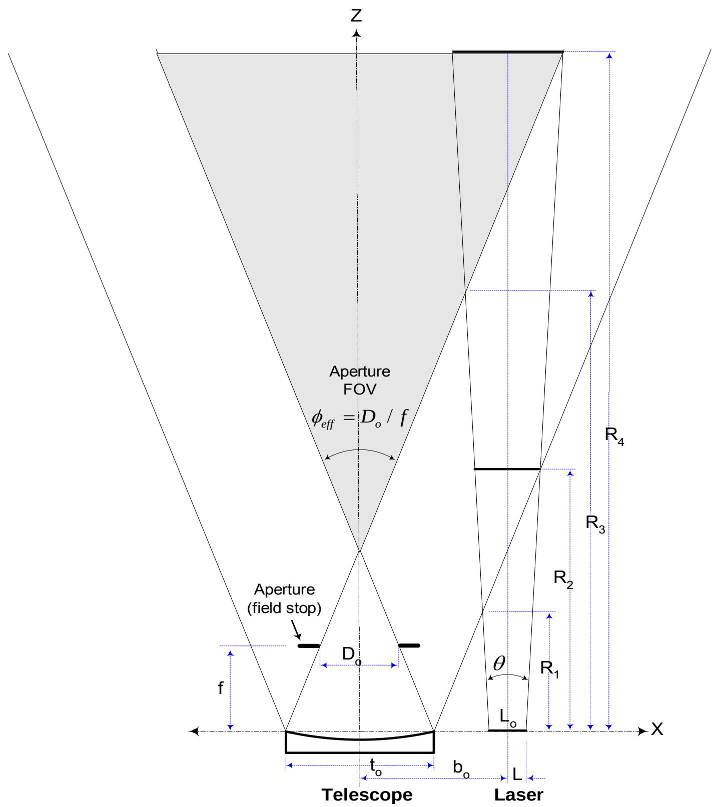

Biaxial Lidar: overlapping between effective FOV of receiver telescope (diameter of t_o) and laser beam (initial diameter L_o) and aperture diameter D_o

minimizing the detected BGP. That can be achieved by moving the commonplace aperture (D_o) center from the origin (f_o) some distance to the left (depend on the object height) and reduces the aperture size from D_o to smaller diameter D_s

$\phi_{eff} = D_o / f_o$ to $\phi_{eff} = D_s / f_s$

Results

Lidar images for range 500m-5km

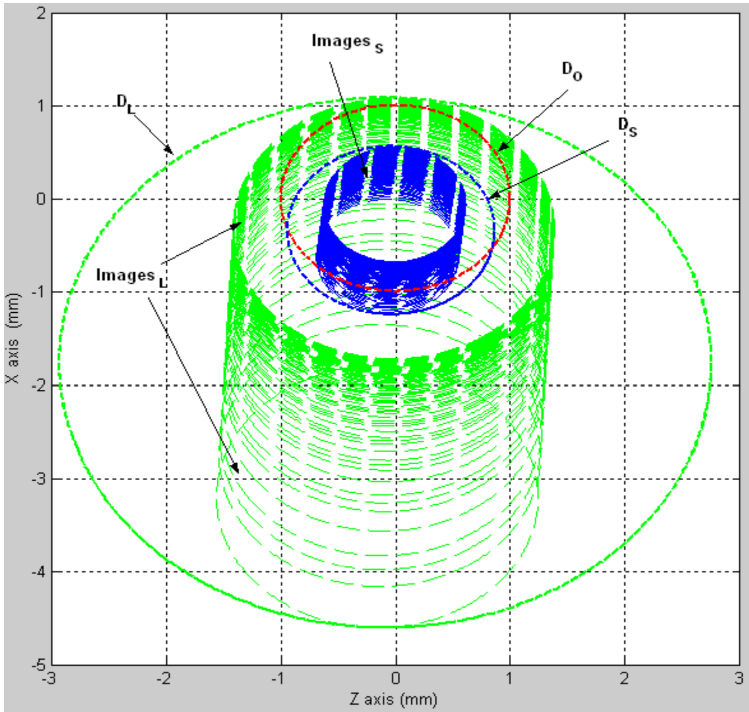

The red circle is the round diaphragm of 2mm diameter
The blue Circle is the proposed diaphragm design

Lidar images for range 5km-25km

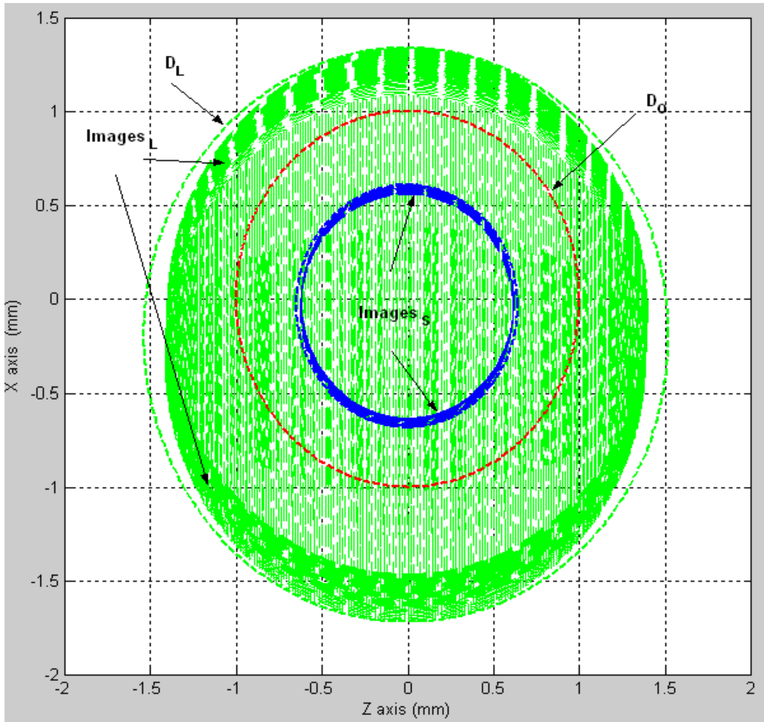

The red circle is the round diaphragm of 2mm diameter
The blue Circle is the proposed diaphragm design

Image's size versus telescope focal length for different lidar ranges. Effective FOV (ϕ_{eff}) is shown no big different in the higher range for a variety of *f*. Normalized ϕ_{eff} with respect to ϕ_{eff} of ($f = 4m$) is also shown

Telescope F	Lidar range 'R' From (km)	To (km)	Aperture diameter D_L (mm)	$\phi_{eff} = D_L / F$ (mrad)	ϕ_{eff} (Norm) %	SNR_{Imp} %
4 m	**0.5**	**5**	**4.7**	**1.175**	**100**	**0**
	5	25	3	0.75	100	0
3 m	**0.5**	**5**	**3.4**	**1.13**	**96**	**2**
	5	25	2.1	0.7	93	3.6
1.7 m	**0.5**	**5**	**1.8**	**1.058**	**90**	**5.4**
	5	25	1.4	0.7	93	3.6
1 m	**0.5**	**5**	**0.85**	**0.85**	**72**	**17.8**
	5	25	0.6	0.6	80	11.8

Conclusion:

- Classical design of lidar receiver subsystem does not account for receiving optics that are placed on line forming an angle with the imaging plane of receiver telescope. (small GF)

- Proposed design attain significant lidar SNR improvements by minimizing the detected sky BGN by setting the receiver round aperture in the proper position with a smaller size.

- Lidar system with small telescope F# is much better in reducing BGS particularly for short distances. Smaller FL to ensure having the minimum FOV that accepts all return signals for the entire ranges.

- results show that a receiver telescope with small F# (1 m) can significantly increase the SNR of factor of 200% as compared to telescope with big F# (> 4 m)

- 200 % SNR improvement is can be translated into equivalent reduction of the required averaging time by a factor of $(1/2)^{1/2}$

- Experiments are planed to test the overlap form factor with the end goal to design an optimized automated variable diaphragm system.

Elastic Backscatter Lidar signal to Noise Ratio Improvement for Daylight Operations: Polarization Selection and Automation

Motivation

- Most lidars are range and sensitivity limited in daylight operation by sky background noise.
- Limits to what can be achieved with narrow band filters have been reached.
- Proposed approach reduces detected sky background by making use of fact that sky background is partially polarized and suitable polarization selection for detection of polarized lidar returns reduces noise.
- - Collecting data without attendance
- - Fast and accurate lidar operations
- - Applicable for Different lidar
- - Globalization.

Sky background suppression geometry

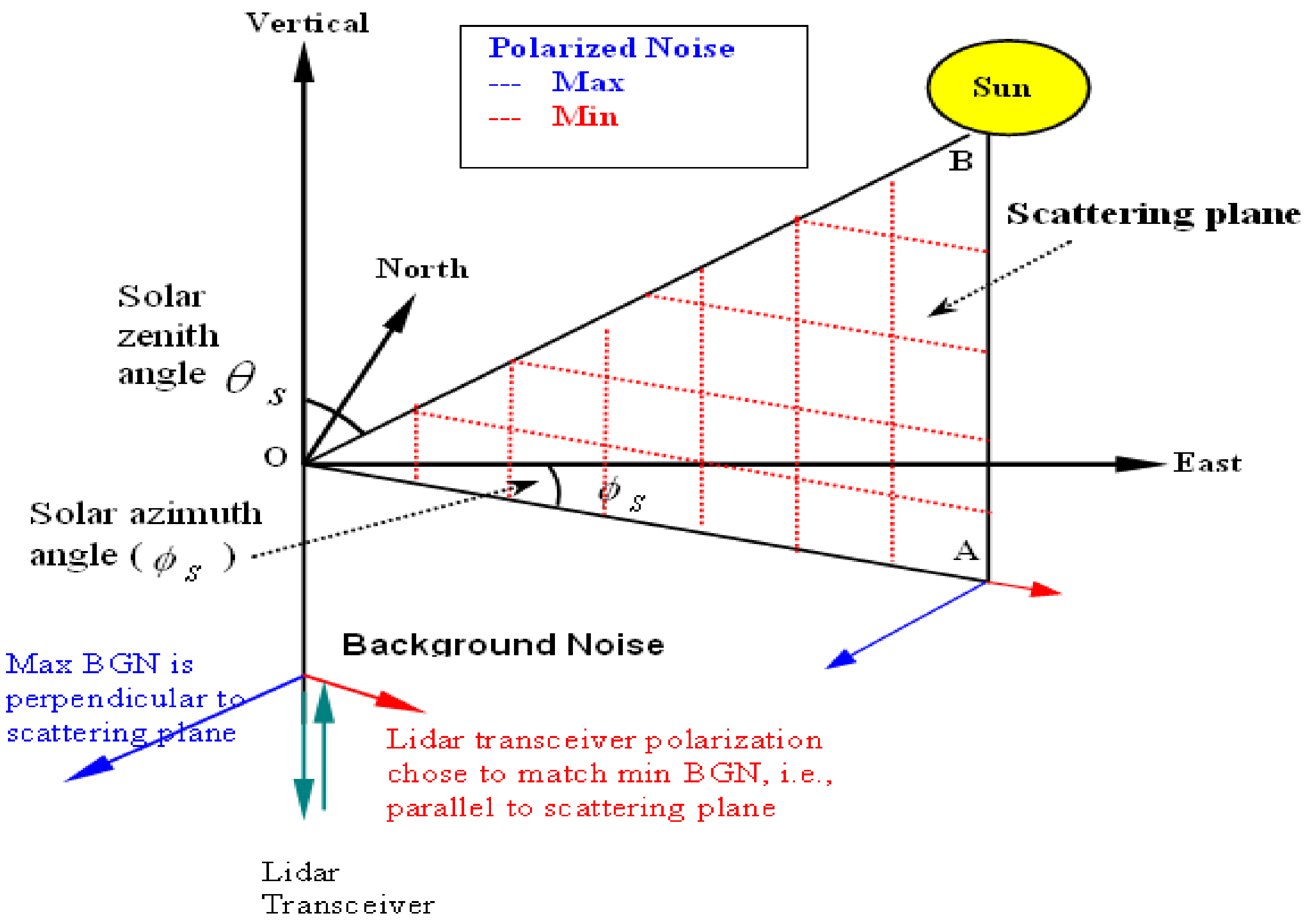

Block diagram of polarization experiment set up
for elastic monostatic biaxial lidar (mobile lidar)

1. **Elastic monostatic biaxial backscatter lidar** system, at CCNY, (longitude 73.94 W, latitude 40.83 N), at 532 nm.
2. The lidar transmitter was a **10 Hz Q-Switched Nd: YAG_** MDL Continuum Surelite laser.
3. The receiver was a **14”** (355.6 mm) diameter CM-1400 Schmidt-Cassegrian telescope with a focal length of 153.9” (3910 mm) coupled to a **PMT R11527P Detector with a 1 nm bandwidth** optical 532F02-25 Andover filter centered at 532 nm wavelength.
4. The lidar output at 532 nm is linearly polarized and has a 0.5 cm beam diameter, 0.5 mrad divergence, pulse energies of 100 mJ, pulse width of 3 ns, **a ½ wave plate rotation of polarization of outgoing signal to match received polarization**

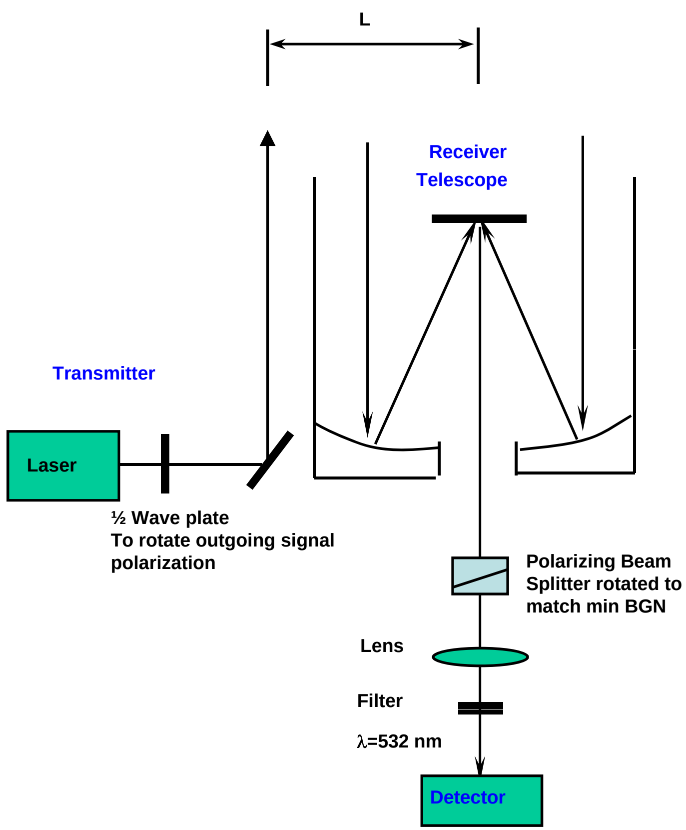

Experimental range dependent SNR for:

Maximum and minimum polarization orientations for

maximum observed G_{imp}

1. SNR improvement of 10 was obtained which resulted in an increase in lidar operating range from 9.38 km to 12.5km is observed (a 34% improvement).
2. Alternatively, for a given lidar range, say 9 km, the SNR improvement was 250%. (6:30PM)
3. Note that, this improvement depends on the angle between the direction of solar radiation and the lidar axis. For vertical lidar this is the solar zenith angle.

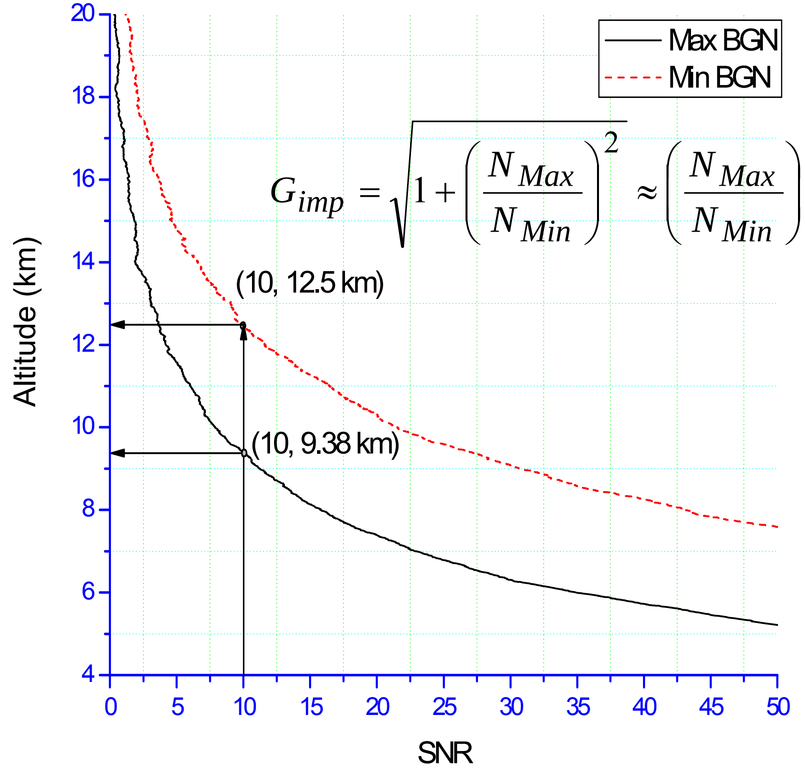

G_{imp} at detection wavelength of 532 nm as function of local time, and solar zenith angle

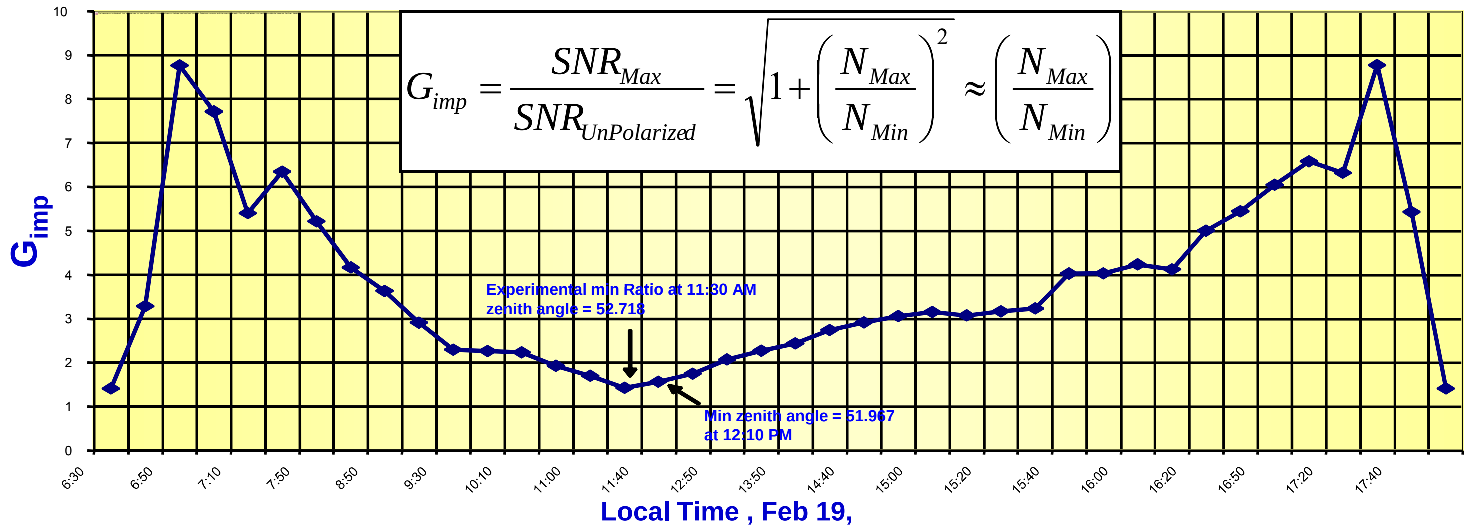

$$G_{imp} = \frac{SNR_{Max}}{SNR_{UnPolarized}} = \sqrt{1+\left(\frac{N_{Max}}{N_{Min}}\right)^2} \approx \left(\frac{N_{Max}}{N_{Min}}\right)$$

G_{imp} vs. Local Time

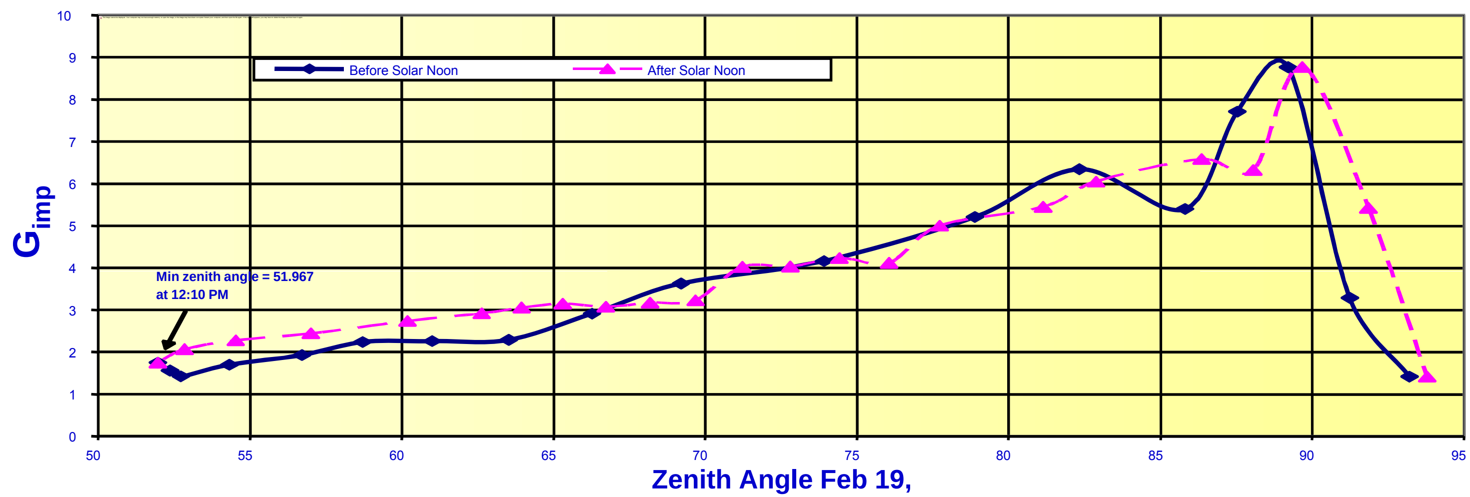

G_{imp} vs. zenith angle

Solar azimuth angle impact on lidar SNR

Polarization orientation for vertical lidar relative to solar azimuth angle needed to achieve minimum BGS

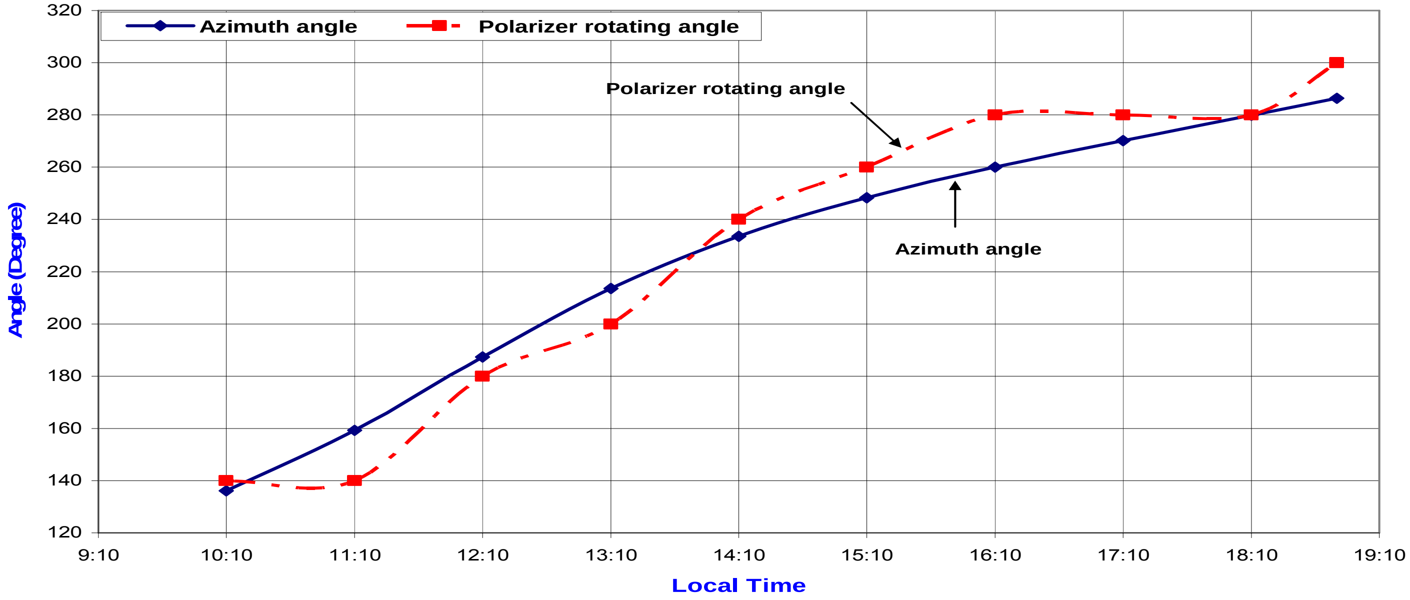

The minimum BGS angle closely tracks the azimuth angle as shown above

•This relationship is important since it allows the system to <u>automatically</u> rotate both the transmitter laser and detector polarizer to the known solar position minimizing the effective BGS.

AUTOMATED CONTROL SYSTEM

TYPICAL INFORMATION EXCHANGE BETWEEN LIDAR SUBSYSTEMS

An appropriate control system, it would then be possible to track the minimum BGS by rotating the detector analyzer and the transmission polarizer **simultaneously** to maximize the SNR,

Achieving the same results as would be done **manually** as described above.

An integration of an **automated** approach is proposed here

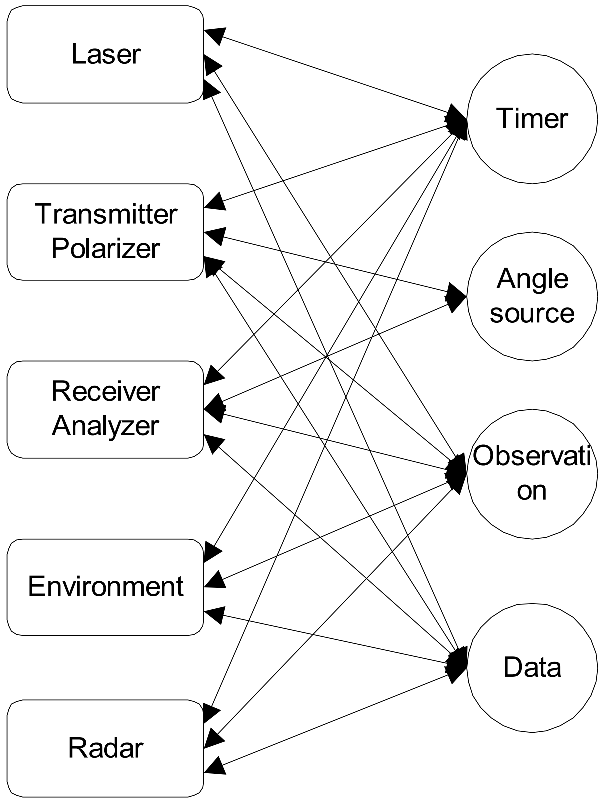

Figure shows a typical information exchange between lidar devices summarizes the interactions used as the basis for the control model operation.

PROPOSED CONTROLLER INSTRUMENTS

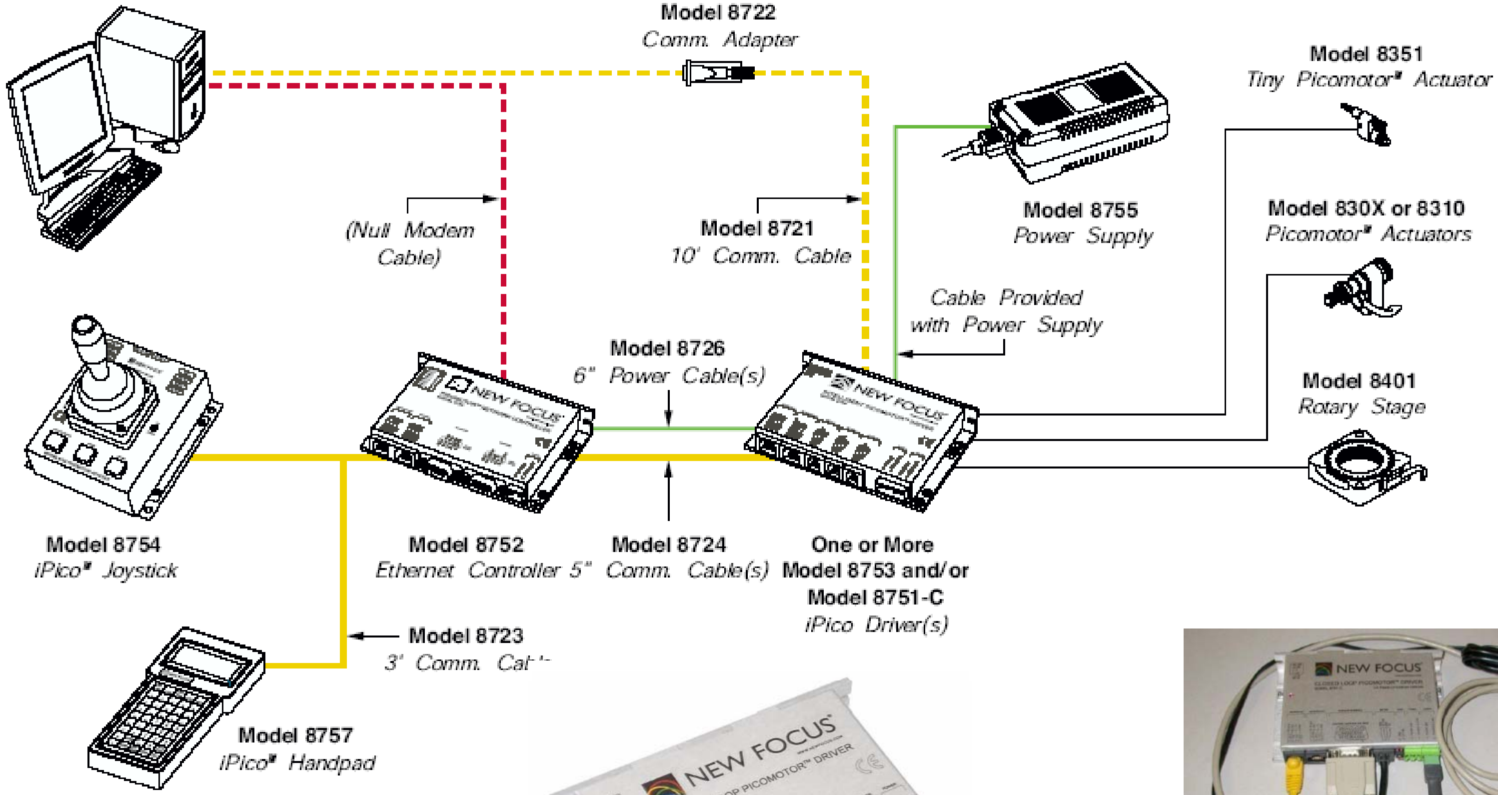

The Intelligent **Picomotor** network can be configured for different motion control applications (User's Guide: Intelligent Picomotor Control Modules)

Model 8751-C Closed- Loop Driver

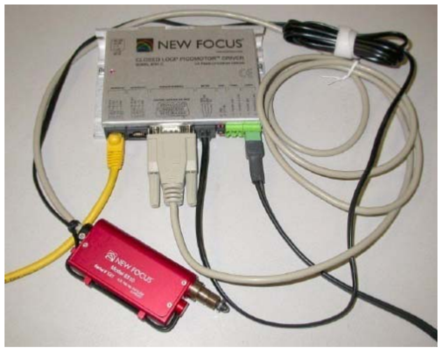

Model 8310 Closed-Loop **Picomotor**

Conclusions

1. SNR improvements obtained for lidar backscatter measurements using polarization selection to eliminate the dominant polarization component can significantly increase the far range SNR as compared to un-polarized detection resulting in range improvements of over 30% for a SNR threshold of 10.
2. This improvement is most significant for large scattering angles, which for vertical pointing lidars, occur near sunrise/sunset.
3. Theoretical models simulate the background skylight within the single scattering approximation was developed and shown to lead to fairly accurate predictions of the SNR improvement.
4. Asymmetric noise reduction was some times observed and could possible explained by an increase in PWV and subsequent modification of aerosol optical depth by hydration.
5. since the polarization axis follows the solar azimuth angle even for high aerosol loading, which may be determined using solar position calculators, it is quite feasible to automate this procedure.
6. Automated control system has been developed.

Fabrication of metal nanoparticles and Laser-induced morphology

Methods:

- ***Metal colloid Prepared by Laser Ablation in aqueous solution***
- ***or PLD***

Target:

- Gold
- Silver
- Zn
- Al
- . Platinum
- Ti
- Si

Metal colloid Prepared by Laser Ablation in aqueous solution

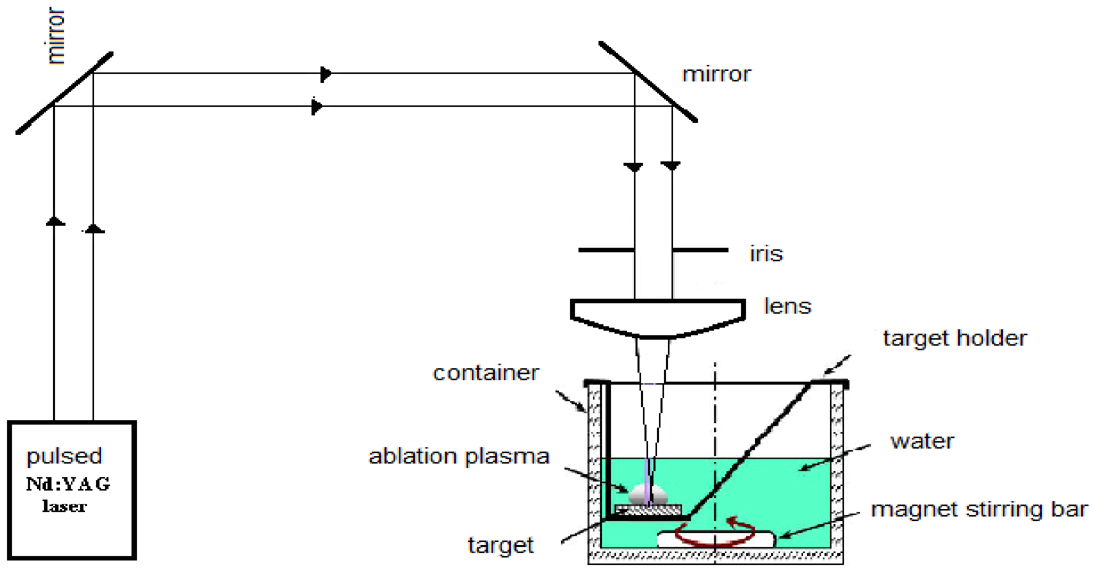

Some examples of metal colloid Prepared by Laser Ablation in aqueous solution

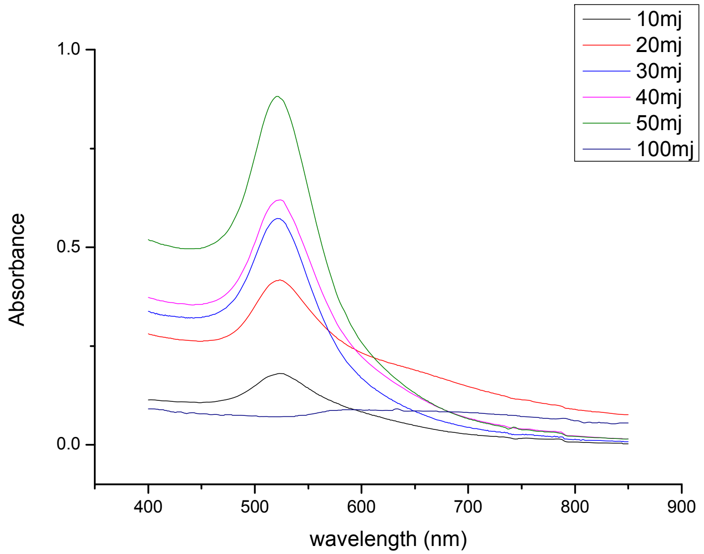

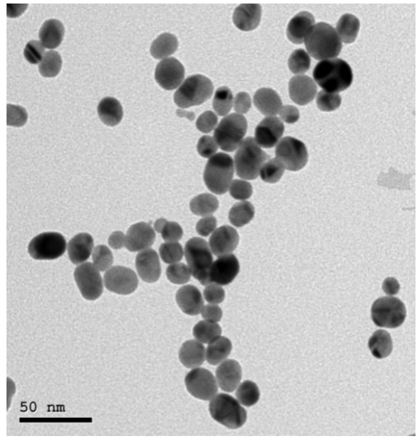

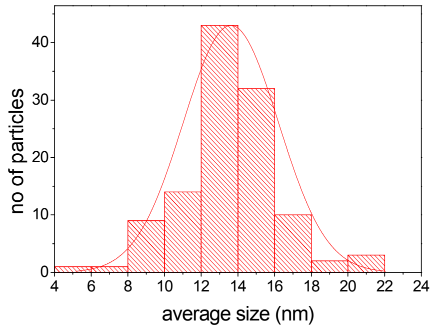

Gold Nanoparticles, E=50mJ, λ=1064nm

absorbance spectrum of gold nanoparticles prepared in pure water at (10-100 mJ

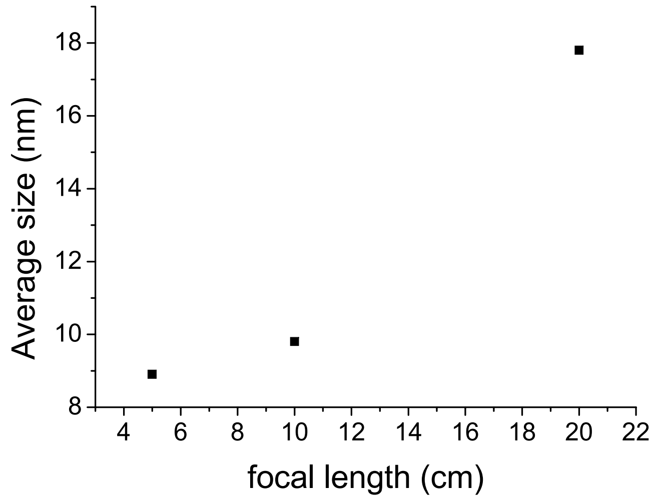

dependence of the focal length on the average size

Parameters that affect nanoparticles fabrication:

- Laser parameters (wavelength, pulse duration, …..)
- Geometrical parameters
- Type of surrounding media
-

Focusing conditions

	Target position	Average size (nm)	Particle distribution (nm)
F=5cm	Above focusing	8.6	8.3-13.6
	At focusing	8.9	14.7-22.7
	Below focusing	7.2	8.6-45
F=10cm	Above focusing	8.3	8.1-14.8
	At focusing	9.8	10-19.3
	Below focusing	7.9	6.6-16.6

The average size and the particle distribution of GNPs at different focal length and target positions.

Pulsed Laser Deposition (PLD)

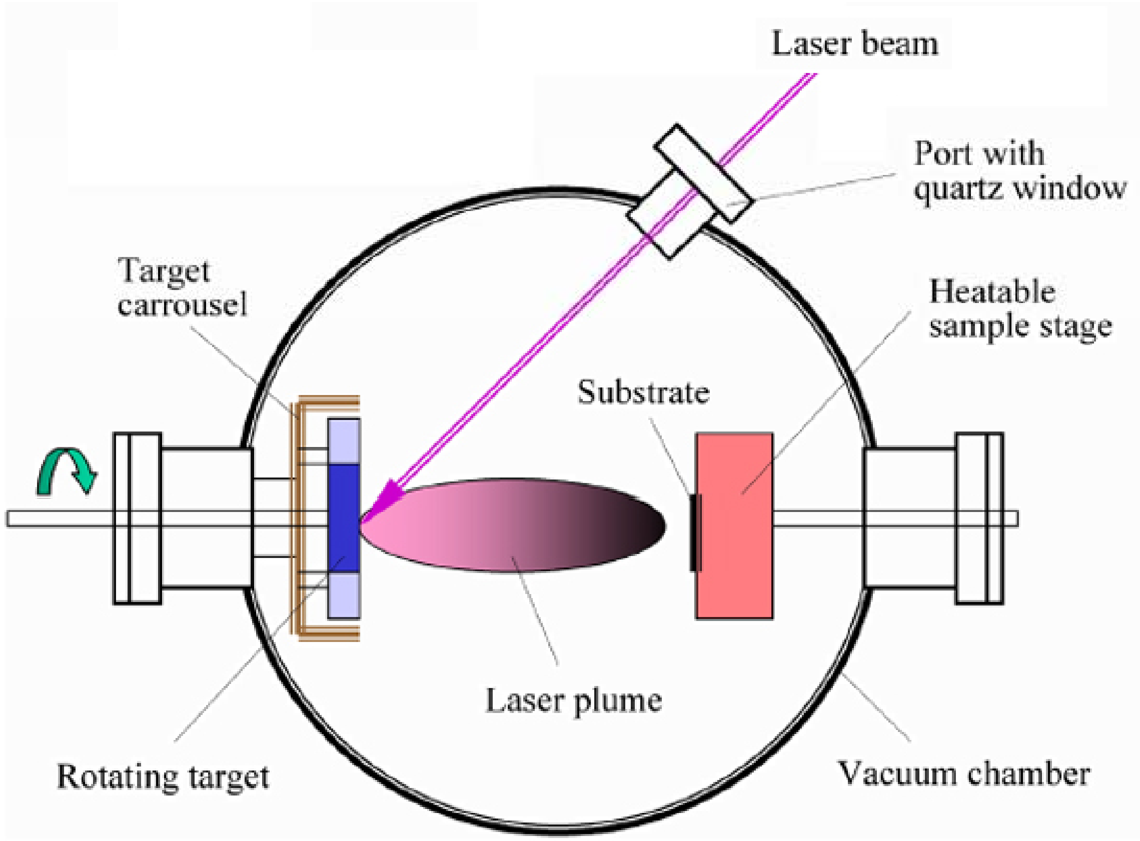

Fabrication of Gas sensors

Zno

Tio

In_2O_3

Thank You…